†Corresponding email address: sandy.herho@email.ucr.edu

Strengthening ITF and Weakening AMOC: Time Series Evidence of Trends and Causal Pathways to Agulhas Variability

Sandy Hardian Susanto Herho[1*],
Katarina Evelyn Permata Herho[2], Iwan Pramesti Anwar[3],
Sri Yudawati Cahyarini[4]

[1*]Department of Earth and Planetary Sciences, University of California, Riverside, 900 University Ave., Riverside, 92521, CA, USA.
[2]Department of Geological Engineering, Trisakti University, Jalan Kyai Tapa 1, West Jakarta, 11440, Special Capital Region of Jakarta, Indonesia.
[3]Oceanography Research Group, Bandung Institute of Technology (ITB), Jalan Ganesha 10, Bandung, 40132, West Java, Indonesia.
[4]Research Center for Climate and Atmosphere (PRIMA), National Research and Innovation Agency (BRIN), Jalan Cisitu Sangkuriang, Bandung, 40135, West Java, Indonesia.

*Corresponding author(s). E-mail(s): sandy.herho@email.ucr.edu;

Abstract

Multi-decadal observations of major ocean circulation systems reveal contrasting trends and complex inter-basin connectivity patterns that challenge traditional conceptualizations of global ocean circulation. Using non-parametric trend analysis, multi-method causality testing, and wavelet coherence techniques, we analyzed volume transport time series spanning 1984–2023 for the Indonesian Throughflow (ITF), Agulhas Current system, and Atlantic Meridional Overturning Circulation (AMOC). The ITF demonstrates statistically significant strengthening, with geostrophic and salinity components increasing by 0.79 and 0.28 Sv decade^{-1}, respectively ($p < 0.05$). Conversely, the AMOC exhibits robust weakening of -1.61 Sv decade^{-1} ($p < 0.0001$), while Agulhas transport shows no significant long-term trends despite substantial interannual variability. Causality analysis reveals four statistically significant pathways linking ITF components to Agulhas variability with lag times of 0–18 months, supported by consensus across maximum cross-correlation, convergent cross mapping, and transfer entropy methods. However, no direct causal connections emerge between either Indo-Pacific system and the AMOC, indicating regional forcing dominance over global-scale coupling on observable timescales. Wavelet coherence analysis identifies dominant annual-scale coupling (0.87–1.30 years) in ITF-Agulhas relationships, with enhanced coherence during major climate events including the 1997–98 El Niño. These findings suggest that contemporary ocean circulation responds primarily to regional forcing mechanisms—intensified Maritime Continent rainfall driving ITF strengthening and weakened North Atlantic convection controlling AMOC decline—rather than operating as a tightly coupled global conveyor belt. The identified statistical relationships provide critical observational constraints for ocean circulation models and highlight the need for sustained monitoring as anthropogenic forcing continues to reshape ocean gateway dynamics.

Keywords: Agulhas Current, Atlantic Meridional Overturning Circulation, Indonesian Throughflow, Ocean transport variability, Statistical causality

1 Introduction

The ocean's meridional overturning circulation constitutes Earth's primary mechanism for redistributing heat from equatorial to polar regions, fundamentally shaping global climate patterns and regional weather systems. This vast circulation network, comprising interconnected currents across all ocean basins, has emerged as a critical focus of climate research due to mounting evidence of ongoing changes in response to contemporary climate forcing. Understanding the variability and trends of major ocean currents—particularly the Atlantic Meridional Overturning Circulation (AMOC), the Indonesian Throughflow (ITF), and the Agulhas Current system—has become essential for characterizing the evolution of the global ocean circulation system.

The modern understanding of ocean circulation rests upon theoretical foundations established over seven decades ago. Stommel (1948) provided the first mathematical explanation for the westward intensification of ocean currents, demonstrating that the latitudinal variation of the Coriolis parameter causes powerful western boundary currents such as the Gulf Stream and Kuroshio Current. This fundamental insight explained why ocean gyres exhibit asymmetric circulation patterns, with swift, narrow currents on western boundaries and broad, diffuse return flows in ocean interiors. Subsequently, Stommel (1961) demonstrated that thermohaline circulation could exist in multiple stable states, introducing the concept that ocean circulation might exhibit different equilibrium modes—a theoretical foundation that continues to inform contemporary ocean circulation research.

Building upon Stommel's theoretical framework, Broecker (1987) conceptualized the global ocean circulation as a "great ocean conveyor belt", a metaphor that captured both scientific and public imagination. This paradigm, elaborated in Broecker (1991), visualized ocean circulation as a continuous loop transporting warm surface waters poleward and cold deep waters equatorward, connecting all ocean basins in a coherent overturning circulation (Fig. 1). While subsequent research has revealed greater complexity than this simplified model suggests (Gordon 1986), the conveyor belt concept established important links between ocean circulation variability and climate changes recorded in paleoclimate archives. The schematic representation in Fig. 1 illustrates this interconnected circulation system, highlighting the three major current systems—the AMOC, ITF, and Agulhas Current—that facilitate inter-basin exchange and maintain planetary-scale heat redistribution.

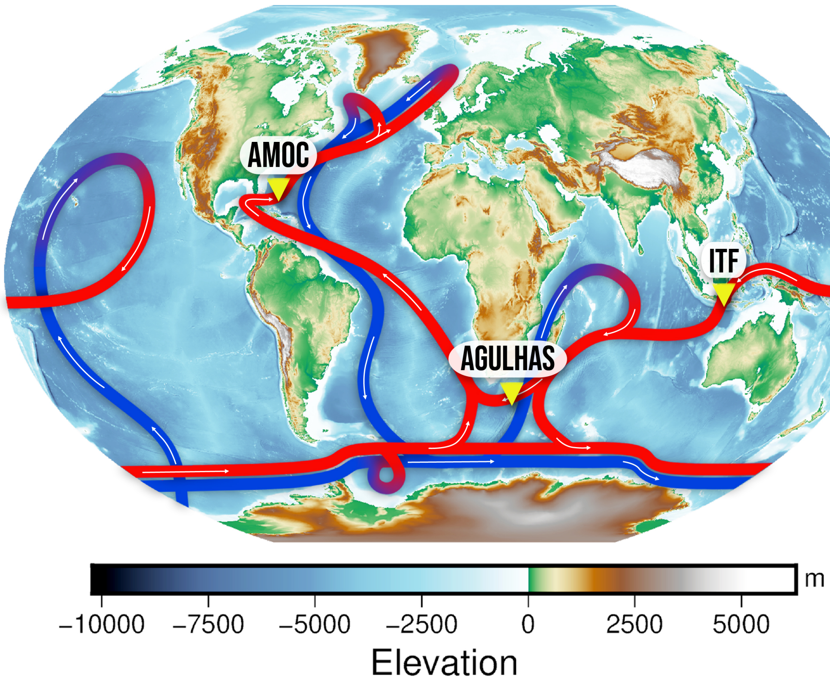

Fig. 1 Schematic representation of the global ocean conveyor belt circulation system, modified from Broecker (1991), overlaid on global topographic and bathymetric relief. Red pathways indicate warm surface currents while blue pathways represent cold deep water circulation. The three major current systems analyzed in this study are labeled: the Atlantic Meridional Overturning Circulation (AMOC), the Indonesian Throughflow (ITF), and the Agulhas Current system. Base map constructed from SRTM15+V2.7 global relief data at 32 km resolution (Tozer et al. 2019) and rendered using PyGMT (Wessel et al. 2019). This simplified representation illustrates the interconnected nature of the global ocean circulation system, wherein changes in one basin can influence circulation patterns across the entire ocean network.

The global overturning circulation depends critically on three major current systems that facilitate inter-ocean exchange and maintain the planetary-scale redistribution of heat and salt. The ITF represents the sole low-latitude pathway connecting the Pacific and Indian Oceans, with significant implications for Indo-Pacific climate dynamics. Early quantitative estimates by Wyrtki (1961) established the seasonal variability of ITF transport, while subsequent observations revealed its role as a "mix master" transforming Pacific waters through intense tidal mixing (Gordon 2005). The landmark INSTANT program provided the first simultaneous measurements across all ITF passages, establishing a mean transport of approximately 15 Sverdrups (1 Sv $\equiv 10^6$ m^3 s^{-1}) with significant interannual variability (Sprintall et al. 2009). Recent studies have documented ITF variability in response to intensified rainfall patterns (Hu and Sprintall 2017), with Feng et al. (2018) synthesizing evidence for long-term changes linked to both regional and global climate forcing.

The Agulhas Current system, Earth's most powerful western boundary current, plays an equally important role in the global circulation through its unique retroflection process. Lutjeharms and van Ballegooyen (1988) provided the seminal description of how the Agulhas Current dramatically turns back upon itself south of Africa, shedding massive rings that carry warm, salty Indian Ocean water into the Atlantic. This "Agulhas leakage" constitutes an important component of the global thermohaline circulation, potentially influencing Atlantic overturning by supplying salt that affects North Atlantic water mass properties (Gordon 1986; Biastoch et al. 2008). Observational programs have revealed the Agulhas Current extends to depths exceeding 2200 meters with transport around 70 Sv, though recent evidence suggests broadening rather than strengthening of the current system (Beal and Elipot 2016). Climate model simulations indicate that poleward shifts in Southern Hemisphere westerlies could modify Agulhas leakage, with potential impacts on Atlantic circulation (Biastoch et al. 2009; Durgadoo et al. 2017).

The AMOC has emerged as a component of global ocean circulation showing significant response to contemporary climate change. Building upon theoretical predictions and modeling studies (Rahmstorf 1995), observational evidence now indicates changes in AMOC strength. Caesar et al. (2018) identified a characteristic sea surface temperature pattern associated with AMOC variability, suggesting approximately 15% weakening since the mid-twentieth century. This finding has been corroborated by proxy reconstructions indicating that current AMOC strength represents relatively weak conditions compared to the past millennium (Thornalley et al. 2018; Caesar et al. 2021).

Recent assessments of AMOC variability have employed diverse methodological approaches. Lenton et al. (2008) identified the AMOC among several components of the Earth system that could undergo significant transitions. Boers (2021) analyzed multiple AMOC proxy records, examining statistical indicators of circulation changes. van Westen et al. (2024) used climate model simulations to investigate AMOC stability, identifying freshwater transport at 34°S as a relevant diagnostic indicator. Ditlevsen and Ditlevsen (2023) applied statistical methods to project potential future AMOC evolution, though their specific timelines remain subject to scientific discussion.

Despite theoretical advances and expanding observational evidence, quantifying ocean circulation changes remains challenging. Direct observations of ocean currents are spatially and temporally limited, necessitating reliance on indirect proxies and model-based reconstructions. The inherent variability of ocean circulation on multiple timescales—from seasonal to multidecadal—complicates detection of long-term trends. Furthermore, systematic differences between climate models and observations, particularly in representing freshwater transport and water mass formation processes, introduce uncertainty in projections. Inter-basin connections through both oceanic pathways and atmospheric teleconnections add complexity, as changes in one region can influence the global circulation system (McGregor et al. 2014; Sun and Thompson 2020).

Given the critical importance of ocean circulation for global climate and the need to better understand ongoing changes, comprehensive statistical analysis of variability and trends in major ocean currents has become essential. This study presents an integrated examination of the ITF, Agulhas Current system, and AMOC, employing multiple statistical techniques to quantify long-term trends and investigate potential relationships between these systems. By analyzing these current systems within a unified statistical framework, we aim to characterize their temporal evolution over recent decades through robust trend analysis, identify and quantify statistical causal pathways and teleconnections between ocean basins, examine the time-frequency characteristics of inter-basin coupling, and assess the degree of connectivity within the global ocean circulation system. Through systematic application of complementary analytical methods—including non-parametric trend detection, multi-method causality analysis, and wavelet coherence—this study provides empirical evidence for understanding how major ocean currents respond to contemporary climate forcing and interact across basin scales.

2 Data and Methods

2.1 Data

Monthly AMOC volumetric transport data were obtained from the Ocean Monitoring Indicator (OMI) of the Copernicus Marine Environment Monitoring Service (CMES), specifically the AMOC timeseries at 26°N from Reanalysis (E.U. Copernicus Marine Service Information (CMEMS) 2024a) spanning January 1993 to December 2023. The monthly mean values from this dataset were utilized for the analysis. This product had been derived using a multi-product approach that combined four distinct ocean reanalyses to construct ensemble-based Ocean Monitoring Indicators for the AMOC. The ensemble approach utilized the Global Ocean Reanalysis and Simulation version 2 volume 4 (GLORYS2V4) from Mercator Ocean (Lellouche et al. 2013), the Copernicus Global Ocean Reanalysis (C-GLORS) from the Centro Euro-Mediterraneo sui Cambiamenti Climatici (CMCC) (Storto et al. 2016), Ocean Reanalysis System 5 (ORAS5) from the European Centre for Medium-Range Weather Forecasts (ECMWF) (Zuo et al. 2017), and the Global Seasonal forecasting system version 5 (GloSea5) (MacLachlan et al. 2015). These four reanalyses were employed to calculate time series of the AMOC maximum transport and climatological mean profiles, which were subsequently combined to form the Global Ocean Ensemble Physics Reanalysis (E.U. Copernicus Marine Service Information (CMEMS) 2024b) with an ensemble mean and spread calculated as twice the ensemble standard deviation in comparison with the RAPID observational AMOC data (Moat et al. 2025; Duchez et al. 2016).

All four reanalysis products were based on the Nucleus for European Modelling of the Ocean (NEMO) model (Madec and NEMO team 2015) implemented on the

ORCA025 grid (0.25° horizontal resolution), with GLORYS2V4 using NEMO version 3.1 with the Louvain-la-Neuve Sea Ice Model version 2 (LIM2) (Rousset et al. 2015; Vancoppenolle et al. 2012) and 75 vertical levels, while C-GLORS and ORAS5 employed NEMO version 3.4 with LIM2, and ORAS5 additionally incorporated version 3.4.1 with surface wave forcing. The models were forced at the sea surface using the ECMWF Re-Analysis Interim (ERA-Interim) (Dee et al. 2011) and bulk formulae, with ERA5 (Hersbach et al. 2020) implemented after 2019, and GLORYS2V4 specifically using Turbulent Kinetic Energy (TKE) altimetry from 1993-2015. Data assimilation methodologies varied across products: GLORYS2V4 employed the Singular Evolutive Extended Kalman (SEEK) filter (Pham et al. 1998) within the Sistema de Asimilación de Mercator version 2 (SAM2) with a 7-day assimilation window; C-GLORS used the three-dimensional variational (3Dvar) (Barker et al. 2004) using the OceanVar system (Dobricic and Pinardi 2008) with a 7-day window; and ORAS5 implemented the NEMO variational data assimilation system (NEMOVAR) (Waters et al. 2015) with 3Dvar multivariate assimilation and a 5-day window. All systems assimilated sea surface temperature (SST), sea level anomalies (SLA), and in situ temperature and salinity profiles T/S(z), with specific SST products including Reynolds SST for GLORYS2V4 and C-GLORS, and Hadley Centre Sea Ice and Sea Surface Temperature version 2 (HadISSTv2) (Rayner et al. 2006) for ORAS5, while sea ice concentrations (SIC) were assimilated using surface nudging techniques in C-GLORS and ORAS5.

ITF volumetric transport data were obtained from the updated estimates of Guo et al. (2023), specifically the monthly time series of total ITF geostrophic transport (ITF-G), temperature component (ITF-T), and salinity component (ITF-S) at the IX1 section between Indonesia and Australia spanning January 1984 to December 2017. The monthly mean values from these datasets were utilized for the analysis. These transport estimates were derived from expendable bathythermograph (XBT) deployments and complementary observational data including mechanical bathythermographs, conductivity-temperature-depth profiles, bottle samples, moored buoys, gliders, and Argo floats, totaling 764,481 profiles with comprehensive bias corrections applied following Cheng et al. (2014) for XBT data and Gouretski and Cheng (2020) for mechanical bathythermograph data.

The ITF transport components were calculated using geostrophic principles through dynamic height integration from a 700 m reference level, with cross-sectional velocities computed via the geostrophic relationship:

$$V_G = \frac{1}{f}\frac{\partial}{\partial L}(D_2 - D_1) \tag{1}$$

, where L represents the distance between neighboring grid boxes and f denotes the Coriolis parameter. The salinity effect was incorporated using two versions of the Institute of Atmospheric Physics (IAP) monthly gridded salinity datasets (Cheng et al. 2020; Tian et al. 2022), which employed feed-forward neural networks and Monte Carlo dropout approaches to reconstruct three-dimensional salinity fields from in situ observations, sea surface temperature, surface winds, and altimeter-derived sea surface height. The transport estimates were decomposed linearly into temperature and salinity components through separate dynamic height calculations, with uncertainty quantification performed using Monte Carlo simulations generating 100 ensemble realizations to propagate data uncertainties into the final transport estimates.

Agulhas Current volume transport data were derived from the comprehensive dataset of Beal and Elipot (2016), who developed 22-year proxy time series spanning September 26, 1992, to December 21, 2014, with 10-day temporal resolution. The transport estimates were constructed by combining three years of in situ measurements from the Agulhas Current Time-series (ACT) mooring array deployed across the current at 34°S with coincident along-track satellite altimeter data from the TOPEX/-Poseidon, Jason-1, and Jason-2 missions. Two distinct transport metrics were utilized: the streamwise jet transport (hereafter referred to as Agulhas Jet), representing the southwestward component integrated to the first maximum beyond the half-width of the mean jet at 110 km offshore, and the boundary layer transport (hereafter referred to as Agulhas Box), representing the net transport integrated across the full 219 km width of the current system.

The proxy time series were generated through nine linear regression models that related local sea surface slope derived from satellite altimetry to transport per unit distance at each ACT mooring location, subsequently interpolated using shape-preserving piecewise cubic Hermite polynomials and integrated horizontally to obtain total transports. The in situ ACT array consisted of seven full-depth current-meter moorings and four current- and pressure-sensor-equipped inverted echo sounders (CPIES), providing comprehensive velocity measurements through acoustic Doppler current profilers, Aquadopp current meters, and geostrophic velocity estimates from CPIES pairs. The resulting proxy estimates explained 55% of the variance for Agulhas Jet and 61% of the variance for Agulhas Box during the three-year validation period, with mean transport values of -84 ± 24 Sv for the jet transport and -77 ± 32 Sv for the boundary layer transport, where negative values indicate southwestward flow. The original 10-day data were preprocessed and aggregated into monthly means to ensure consistent temporal resolution with the ITF and AMOC datasets for comparative analysis.

Figure 2 presents the complete time series of volume transport data used in this study, spanning the period from 1984 to 2022. Figure 2 (upper panel) displays the ITF components, which exhibit substantial interannual and decadal variability with magnitudes typically ranging between -10 and +20 Sv. The middle panel shows the Agulhas Current transport metrics, where both the Agulhas Box and Agulhas Jet demonstrate strong southwestward flow with mean values around -80 to -100 Sv and notable variability throughout the record period. The bottom panel illustrates the AMOC strength, characterized by generally positive values between 10 and 25 Sv with pronounced fluctuations and some evidence of decadal-scale trends. All datasets have been processed to monthly resolution to enable direct comparison.

2.2 Methods

2.2.1 Descriptive Statistical Analysis

Comprehensive descriptive statistics were computed for all oceanic volume transport time series to characterize their distributional properties and variability patterns. The

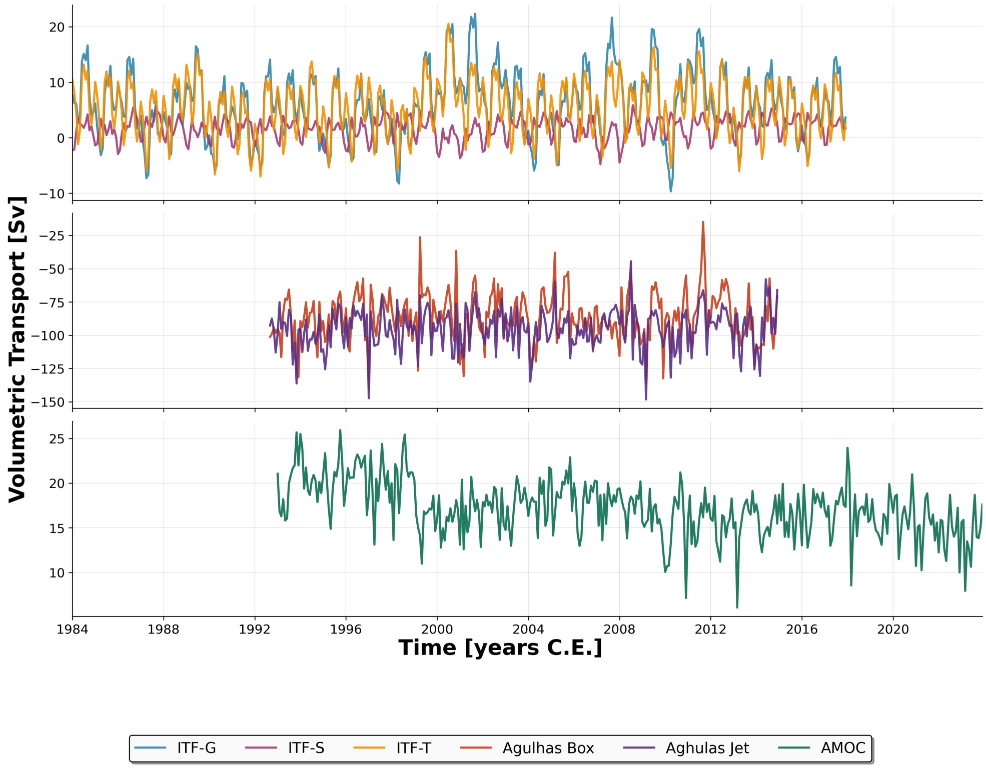

Fig. 2 Time series of oceanic volume transport data from 1984 to 2022. Upper panel: ITF components including Geostrophic (ITF-G, blue), Salinity (ITF-S, purple), and Temperature (ITF-T, orange) transports. Middle panel: Agulhas Current transports showing Agulhas Box (red) and Agulhas Jet (purple) components. Lower panel: AMOC (green). All data are presented at monthly resolution with transport units in Sv. For ITF, positive values indicate transport toward the Indian Ocean. For Agulhas Current, negative values represent the characteristic southwestward flow. For AMOC, values indicate the strength of the meridional overturning circulation.

statistical analyses were performed using Python with the NumPy (Harris et al. 2020), pandas (McKinney 2011), and SciPy (Virtanen et al. 2020) libraries.

For each transport variable, measures of central tendency and dispersion were calculated to characterize the typical values and variability. The arithmetic mean ($\bar{x}$) and median ($\tilde{x}$) were computed as:

$$\bar{x} = \frac{1}{n}\sum_{i=1}^{n} x_i, \tag{2}$$

$$\tilde{x} = \begin{cases} x_{(n+1)/2}, & \text{if } n \text{ is odd,} \\ \frac{x_{n/2} + x_{(n/2)+1}}{2}, & \text{if } n \text{ is even,} \end{cases} \tag{3}$$

where x_i represents individual transport observations and n is the sample size. The standard deviation (σ) was calculated as:

$$\sigma = \sqrt{\frac{1}{n-1}\sum_{i=1}^{n}(x_i - \bar{x})^2}. \tag{4}$$

Additionally, the interquartile range (IQR) was computed as:

$$\mathrm{IQR} = Q_3 - Q_1, \tag{5}$$

where Q_1 and Q_3 represent the first and third quartiles, respectively.

To account for potential outliers and provide outlier-resistant estimates, robust statistical measures were employed. The median absolute deviation (MAD) was calculated using the SciPy's `median_abs_deviation` function:

$$\mathrm{MAD} = \mathrm{median}(|x_i - \tilde{x}|). \tag{6}$$

Trimmed means at 10% ($\bar{x}_{0.1}$) and 20% ($\bar{x}_{0.2}$) levels were computed using the SciPy's `trim_mean` function, which removes the specified proportion of extreme values from both tails before calculating the mean:

$$\bar{x}_\alpha = \frac{1}{n(1-2\alpha)}\sum_{i=\lfloor n\alpha\rfloor+1}^{n-\lfloor n\alpha\rfloor} x_{(i)}, \tag{7}$$

where α represents the trimming proportion (0.1 or 0.2) and $x_{(i)}$ denotes the i-th order statistic.

Distribution shape parameters were assessed to understand the symmetry and tail behavior of the transport distributions. The skewness (γ_1) and excess kurtosis (γ_2) were calculated using the SciPy's `skew` and `kurtosis` functions:

$$\gamma_1 = \frac{\frac{1}{n}\sum_{i=1}^{n}(x_i - \bar{x})^3}{\sigma^3}, \tag{8}$$

$$\gamma_2 = \frac{\frac{1}{n}\sum_{i=1}^{n}(x_i - \bar{x})^4}{\sigma^4} - 3. \tag{9}$$

The coefficient of variation (CV) was computed as:

$$\mathrm{CV} = \frac{\sigma}{|\bar{x}|}. \tag{10}$$

Percentile analysis was conducted to characterize the distribution of volume transport values across their full range. Percentiles P_k for $k \in \{1, 5, 10, 25, 75, 90, 95, 99\}$ were calculated using the pandas' `quantile` method, where P_k represents the value below which $k\%$ of the observations fall. For each time series, the minimum and maximum values were identified along with their corresponding temporal occurrences to characterize extreme transport events.

All statistical computations were performed after removing missing values (NaN) from the datasets. The distributional characteristics were assessed through the combination of classical parametric measures (mean, standard deviation) and robust non-parametric statistics (median, MAD, trimmed means) to provide a comprehensive understanding of the transport variability patterns. The skewness values were interpreted as symmetric ($|\gamma_1| < 0.5$), moderately skewed ($0.5 \leq |\gamma_1| < 1.0$), or highly skewed ($|\gamma_1| \geq 1.0$), while kurtosis values indicated platykurtic ($\gamma_2 < 0$), mesokurtic ($\gamma_2 \approx 0$), or leptokurtic ($\gamma_2 > 0$) distributions.

2.2.2 Annual Cycle Analysis

The seasonal variability of volume transport was characterized through annual cycle analysis performed on all time series. Monthly climatological statistics were computed to quantify the seasonal modulation of transport volumes and identify peak transport periods. The analyses were implemented using pandas groupby operations (McKinney 2011) and NumPy array computations (Harris et al. 2020).

For each transport variable, the monthly climatological mean ($\bar{x}_m$) was calculated by grouping observations by calendar month:

$$\bar{x}_m = \frac{1}{n_m} \sum_{i=1}^{n_m} x_{m,i}, \tag{11}$$

where m denotes the month (1-12), n_m is the number of observations in month m, and $x_{m,i}$ represents the i-th observation in month m. The monthly standard deviation (σ_m) was computed as:

$$\sigma_m = \sqrt{\frac{1}{n_m - 1} \sum_{i=1}^{n_m} (x_{m,i} - \bar{x}_m)^2}. \tag{12}$$

To quantify the uncertainty in the monthly climatological means, the standard error (SE_m) was calculated for each month:

$$SE_m = \frac{\sigma_m}{\sqrt{n_m}}. \tag{13}$$

This measure provides confidence bounds for the monthly mean estimates, accounting for both the variability within each month and the sample size.

The annual mean transport ($\bar{X}_{\text{annual}}$) was computed as the average of the twelve monthly climatological means:

$$\bar{X}_{\text{annual}} = \frac{1}{12} \sum_{m=1}^{12} \bar{x}_m. \tag{14}$$

The seasonal amplitude (A_{seasonal}), representing the range of seasonal variation, was calculated as:

$$A_{\text{seasonal}} = \max_m(\bar{x}_m) - \min_m(\bar{x}_m), \tag{15}$$

where $\max_m$ and $\min_m$ denote the maximum and minimum values across all twelve monthly means, respectively.

To assess the relative strength of seasonal variability, the coefficient of variation for the seasonal cycle (CV_{seasonal}) was computed:

$$CV_{\text{seasonal}} = \frac{\sigma_{\text{monthly}}}{\bar{X}_{\text{annual}}}, \times 100\% \tag{16}$$

where $\sigma_{monthly}$ is the standard deviation of the twelve monthly climatological means:

$$\sigma_{\text{monthly}} = \sqrt{\frac{1}{11}\sum_{m=1}^{12}(\bar{x}_m - \bar{X}_{\text{annual}})^2}. \tag{17}$$

The timing of maximum and minimum transport was identified by determining the months corresponding to the highest and lowest climatological mean values. These extrema provide insight into the seasonal forcing mechanisms affecting each current system. The annual cycle analysis was performed after parsing temporal information from the datasets using pandas datetime functionality, with missing values excluded from all calculations. The resulting monthly climatologies characterize the mean seasonal behavior of each transport component, while the standard errors quantify the inter-annual variability within each month.

2.2.3 Trend Analysis

Long-term trends in volumetric transport were quantified using the Theil-Sen estimator (Theil 1950; Sen 1968), a robust non-parametric regression method that is resistant to outliers and does not assume normally distributed residuals. The Theil-Sen regression was implemented using scikit-learn's `TheilSenRegressor` (Pedregosa et al. 2011) with 300 maximum iterations and a tolerance of 10^{-2}. Statistical significance of the trends was assessed using the Mann-Kendall test, a non-parametric method for monotonic trend detection (Mann 1945; Kendall 1975).

The Theil-Sen estimator calculates the slope (β_{TS}) as the median of all pairwise slopes between data points:

$$\beta_{TS} = \text{median}\left\{\frac{x_j - x_i}{t_j - t_i}\right\}_{i<j}, \tag{18}$$

where x_i and x_j are transport observations at times t_i and t_j, respectively, for all pairs where $i < j$. The intercept (α_{TS}) is then computed as:

$$\alpha_{TS} = \text{median}\{x_i - \beta_{TS} t_i\}. \tag{19}$$

The statistical significance of detected trends was evaluated using the Mann-Kendall test. The test statistic S is calculated as:

$$S = \sum_{i=1}^{n-1} \sum_{j=i+1}^{n} \mathrm{sgn}(x_j - x_i), \tag{20}$$

where $\mathrm{sgn}(\cdot)$ is the sign function. Under the null hypothesis of no trend, the variance of S is:

$$\mathrm{Var}(S) = \frac{n(n-1)(2n+5)}{18} \tag{21}$$

, where n is the number of observations. The standardized test statistic Z is computed as:

$$Z = \begin{cases} \frac{S-1}{\sqrt{\mathrm{Var}(S)}}, & \text{if } S > 0, \\ 0, & \text{if } S = 0, \\ \frac{S+1}{\sqrt{\mathrm{Var}(S)}} & \text{if } S < 0. \end{cases} \tag{22}$$

The two-tailed p-value for the Mann-Kendall test was calculated using the standard normal distribution implemented in SciPy:

$$p = 2 \times (1 - \Phi(|Z|)), \tag{23}$$

where $\Phi(\cdot)$ is the cumulative distribution function of the standard normal distribution. Trends were considered statistically significant at the $\alpha = 0.05$ level. For each transport time series, the linear trend was expressed both as an annual rate of change (Sv/year) and as a decadal trend.

The analysis was performed on all available data points after removing missing values, with the temporal coverage varying among different transport components. All trends were visualized over a standardized time axis spanning 1984-2023 to facilitate inter-comparison, though actual data availability differed among the time series. The combination of robust regression through the Theil-Sen estimator and non-parametric significance testing via the Mann-Kendall test provides a comprehensive assessment of long-term trends that is resistant to outliers and does not rely on parametric assumptions about the data distribution.

2.2.4 Statistical Causality Analysis

The statistical causal relationships between ocean transport systems were investigated using a multi-method approach to identify robust teleconnections across the ITF-Agulhas-AMOC pathway. Three complementary causality metrics were employed to capture both linear and nonlinear dependencies (Runge et al. 2019), with statistical significance assessed through block bootstrap resampling that preserves the autocorrelation structure inherent in oceanographic time series (Politis and Romano 1994). Prior to causality analysis, all transport time series were aligned to their common temporal overlap period to ensure consistent comparison. The alignment procedure was implemented using pandas `datetime` functionality, with linear interpolation applied to fill minor gaps (maximum three consecutive values) followed by removal of any remaining missing values. This preprocessing step was essential to maintain temporal correspondence across the different ocean basins while preserving the integrity of the causal signal propagation.

The maximum cross-correlation (MCC) method was employed to identify linear lagged relationships between transport time series (Bretherton et al. 1992). For two standardized time series $x(t)$ and $y(t)$, the cross-correlation function at lag τ is defined as:

$$r_{xy}(\tau) = \begin{cases} \frac{1}{n-\tau}\sum_{t=1}^{n-\tau} x'(t)y'(t+\tau), & \tau \geq 0, \\ \frac{1}{n+\tau}\sum_{t=1-\tau}^{n} x'(t)y'(t+\tau), & \tau < 0, \end{cases} \tag{24}$$

where $x'(t) = (x(t) - \bar{x})/\sigma_x$ and $y'(t) = (y(t) - \bar{y})/\sigma_y$ represent the standardized series. The maximum cross-correlation and corresponding optimal lag were determined as:

$$\text{MCC} = \max_{\tau \in [-\tau_{\max}, \tau_{\max}]} |r_{xy}(\tau)|, \tag{25}$$

$$\tau_{\text{opt}} = \arg \max_{\tau \in [-\tau_{\max}, \tau_{\max}]} |r_{xy}(\tau)|, \tag{26}$$

where $\tau_{\max} = 24$ months was selected to capture seasonal to interannual propagation timescales. Positive lags indicate that variations in x lead those in y, consistent with downstream signal propagation. The MCC analysis was implemented using NumPy's correlation functions, providing a computationally efficient assessment of linear teleconnections. This method is particularly effective for detecting coherent phase relationships in ocean transport, though it may underestimate causality in systems with significant nonlinear dynamics.

To capture nonlinear causal relationships that may be missed by correlation-based methods, convergent cross mapping (CCM) was implemented following the framework of Sugihara et al. (2012). CCM tests whether historical values of time series x can be reconstructed from the attractor manifold of time series y, indicating that x causally influences y. The method employs time-delay embedding to reconstruct the system's attractor:

$$\mathbf{y}_E(t) = [y(t), y(t-\tau), y(t-2\tau), ..., y(t-(E-1)\tau)], \tag{27}$$

where E is the embedding dimension and τ is the delay. For each embedded point $\mathbf{y}_E(t)$, the $E+1$ nearest neighbors are identified in the reconstructed state space, with predictions of $x(t)$ generated through distance-weighted averaging:

$$\hat{x}(t|M_y) = \sum_{i=1}^{E+1} w_i x(t_i), \tag{28}$$

where $w_i = \exp(-d_i)/\sum_j \exp(-d_j)$ are exponential weights based on Euclidean distances d_i in the embedded space, and M_y denotes the attractor manifold of y. The CCM strength is quantified as the correlation between predicted and observed values:

$$\rho_{CCM} = \text{cor}[\hat{x}(t|M_y), x(t)]. \tag{29}$$

The analysis employed $E = 3$ based on false nearest neighbor analysis (Kennel et al. 1992) and $\tau = 1$ month, with library sizes ranging from 10% to 90% of the time series length to test for convergence. The implementation utilized NumPy for array operations and custom neighbor-finding algorithms optimized for the moderate-dimensional embedded spaces. CCM is particularly powerful for detecting causality in coupled nonlinear systems like ocean circulation, where feedback loops and threshold behaviors may obscure linear relationships (Ye et al. 2015).

Information-theoretic causality was assessed using transfer entropy (TE), which quantifies the reduction in uncertainty about the future of y given knowledge of the past of x beyond what is already known from the past of y itself (Schreiber 2000). The TE from x to y is defined as:

$$TE_{x\to y} = \sum_{y_{t+1}, y_t^k, x_t^k} p(y_{t+1}, y_t^k, x_t^k) \log \frac{p(y_{t+1}|y_t^k, x_t^k)}{p(y_{t+1}|y_t^k)}, \tag{30}$$

where $y_t^k = [y_t, y_{t-1}, ..., y_{t-k+1}]$ and $x_t^k = [x_t, x_{t-1}, ..., x_{t-k+1}]$ represent the k-length history vectors. In practice, this can be rewritten using mutual information:

$$TE_{x\to y} = I(y_{t+1}; x_t^k | y_t^k). \tag{31}$$

The continuous transport values were discretized into 10 bins using pandas' `cut` function with equal-frequency binning to ensure adequate sampling of each state. The mutual information terms were calculated using scikit-learn's `mutual_info_score`, with $k = 1$ to capture direct monthly influences. To account for differences in signal complexity, the TE values were normalized by the entropy of the target variable:

$$\overline{TE}_{x\to y} = \frac{TE_{x\to y}}{H(y_{t+1})}, \tag{32}$$

where $H(y_{t+1}) = -\sum_i p(y_i) \log p(y_i)$ is the Shannon entropy. This normalization facilitates comparison across transport components with different variability characteristics. TE provides a model-free measure of directional information flow, making it particularly suitable for detecting causal relationships in complex ocean circulation systems where the underlying dynamics may be unknown or highly nonlinear (Paluš and Vejmelka 2007).

The statistical significance of all causality metrics was assessed using block bootstrap resampling, which preserves the temporal dependence structure critical in oceanographic time series (Efron and Tibshirani 1994). The block length was adaptively determined based on the decorrelation timescale:

$$\tau_{\text{decorr}} = \min\{t : \rho_{xx}(t) < e^{-1}\}, \tag{33}$$

where $\rho_{xx}(t)$ is the autocorrelation function. The block length was set as $L_{\text{block}} = \min(30, \max(5, 2\tau_{\text{decorr}}))$ to balance preservation of correlation structure with sufficient randomization. For each causality metric, 500-1000 surrogate time series were generated by block permutation of the target series while keeping the source series fixed. The empirical p-value was calculated as:

$$p = \frac{1}{N_{\text{surr}}} \sum_{i=1}^{N_{\text{surr}}} \mathbb{I}[M_{\text{surr},i} \geq M_{\text{obs}}], \tag{34}$$

where M_{obs} is the observed metric value, $M_{\text{surr},i}$ is the metric for the i-th surrogate, and $\mathbb{I}[\cdot]$ is the indicator function. Statistical significance was assessed at the $\alpha = 0.05$ level, with additional notation for highly significant results ($\alpha = 0.01$).

To identify robust causal pathways, a consensus approach was implemented combining evidence from all three methods. For each tested pathway, a consensus score was calculated as:

$$C = \sum_{m \in \{\text{MCC, CCM, TE}\}} \mathbb{I}[p_m < 0.05], \tag{35}$$

ranging from 0 (no significant evidence) to 3 (unanimous significant evidence). Pathways with $C \geq 2$ were considered dominant, indicating robust causality supported by multiple independent methodological approaches. This multi-method consensus framework provides greater confidence in identifying genuine ocean teleconnections while reducing the likelihood of spurious detections that might arise from any single method's limitations or assumptions (Runge et al. 2019).

2.2.5 Wavelet Coherence Analysis

To further investigate the time-frequency characteristics of the statistically significant causal pathways identified in the previous analysis, wavelet coherence analysis was performed following the theoretical framework of Torrence and Compo (1998) and Grinsted et al. (2004). This method extends traditional coherence analysis into the time-frequency domain, enabling identification of transient and scale-dependent relationships between ocean transport time series.

The continuous wavelet transform (CWT) emerges from the need to analyze non-stationary signals where frequency content varies with time. Beginning with the Fourier transform:

$$\hat{x}(\omega) = \int_{-\infty}^{\infty} x(t) e^{-i\omega t} dt, \tag{36}$$

we recognize its limitation in providing no temporal localization. The short-time Fourier transform addresses this through windowing, but suffers from fixed time-frequency resolution. The wavelet transform overcomes this limitation through scale-dependent windowing.

The continuous wavelet transform of a time series $x(t) \in L^2(\mathbb{R})$ with respect to a mother wavelet $\psi(t)$ is defined as:

$$W_x(s, \tau) = \langle x, \psi_{s,\tau} \rangle = \frac{1}{\sqrt{s}} \int_{-\infty}^{\infty} x(t) \psi^* \left(\frac{t - \tau}{s} \right) dt \tag{37}$$

, where $s > 0$ is the scale parameter, $\tau \in \mathbb{R}$ is the translation parameter, and ψ^* denotes the complex conjugate. The normalization factor $1/\sqrt{s}$ ensures energy preservation across scales:

$$\|\psi_{s,\tau}\|^2 = \int_{-\infty}^{\infty} \left| \frac{1}{\sqrt{s}} \psi\left(\frac{t-\tau}{s}\right) \right|^2 dt = \|\psi\|^2. \tag{38}$$

For this analysis, the analytic Morlet wavelet was employed:

$$\psi(t) = \pi^{-1/4} e^{i\omega_0 t} e^{-t^2/2} \tag{39}$$

, where ω_0 is the central frequency. To satisfy the admissibility condition:

$$C_\psi = \int_0^\infty \frac{|\hat{\psi}(\omega)|^2}{\omega} d\omega < \infty, \tag{40}$$

which requires $\hat{\psi}(0) = 0$, a correction term is needed. However, for $\omega_0 \geq 5$, the correction becomes negligible (Farge 1992). The Fourier transform of the Morlet wavelet is:

$$\hat{\psi}(\omega) = \pi^{-1/4} e^{-(\omega-\omega_0)^2/2}. \tag{41}$$

Setting $\omega_0 = 6$ provides optimal balance between time and frequency localization. The time-frequency resolution follows the Heisenberg uncertainty principle:

$$\Delta t \cdot \Delta\omega \geq \frac{1}{2}, \tag{42}$$

where for the Morlet wavelet:

$$\Delta t = \frac{s}{\sqrt{2}}, \quad \Delta\omega = \frac{1}{\sqrt{2}s}. \tag{43}$$

The relationship between scale s and Fourier period λ for the Morlet wavelet is:

$$\lambda = \frac{4\pi s}{\omega_0 + \sqrt{2 + \omega_0^2}}. \tag{44}$$

For $\omega_0 = 6$, this simplifies to $\lambda \approx 1.03s$.

The cross-wavelet transform between two time series $x(t)$ and $y(t)$ is:

$$W_{xy}(s,\tau) = W_x(s,\tau) W_y^*(s,\tau) = |W_{xy}(s,\tau)| e^{i\phi_{xy}(s,\tau)}, \tag{45}$$

where the cross-wavelet power is $|W_{xy}(s,\tau)|^2$ and the phase is:

$$\phi_{xy}(s,\tau) = \arg(W_{xy}(s,\tau)) = \tan^{-1}\left(\frac{\Im(W_{xy}(s,\tau))}{\Re(W_{xy}(s,\tau))}\right). \tag{46}$$

The wavelet coherence requires smoothing to achieve statistical stability. Following Torrence and Webster (1999), we define the smoothed wavelet spectra:

$$\langle W_x(s,\tau) \rangle = S_s(S_t(W_x(s,\tau))), \tag{47}$$

where the time smoothing operator is:

$$S_t(W(s,\tau)) = \int_{-\infty}^{\infty} W(s,\tau')G_t(\tau-\tau';s)d\tau', \tag{48}$$

with Gaussian kernel:

$$G_t(t;s) = \frac{1}{\sqrt{2\pi}s/2}e^{-t^2/(2(s/2)^2)}. \tag{49}$$

The scale smoothing operator is:

$$S_s(W(s,\tau)) = \int_0^{\infty} W(s',\tau)\Pi_s(s,s')ds', \tag{50}$$

where Π_s is a boxcar function:

$$\Pi_s(s,s') = \begin{cases} \frac{1}{0.6s}, & |s-s'| \leq 0.3s \\ 0, & \text{otherwise} \end{cases}. \tag{51}$$

The wavelet coherence is then:

$$R^2(s,\tau) = \frac{|\langle W_{xy}(s,\tau)\rangle|^2}{\langle |W_x(s,\tau)|^2\rangle\langle |W_y(s,\tau)|^2\rangle}, \tag{52}$$

which satisfies $0 \leq R^2(s,\tau) \leq 1$ by the Cauchy-Schwarz inequality.

Statistical significance testing employs Monte Carlo methods with surrogate data. Assuming the time series follow AR(1) processes:

$$x_t = \alpha x_{t-1} + \epsilon_t, \tag{53}$$

where $\epsilon_t \sim \mathcal{N}(0,\sigma^2)$ and the lag-1 autocorrelation is:

$$\alpha = \frac{\sum_{t=1}^{N-1}(x_t-\bar{x})(x_{t+1}-\bar{x})}{\sum_{t=1}^{N}(x_t-\bar{x})^2}. \tag{54}$$

The theoretical power spectrum of an AR(1) process is:

$$P_{\mathrm{AR(1)}}(f) = \frac{\sigma^2(1-\alpha^2)}{|1-\alpha e^{-2\pi i f\Delta t}|^2}, \tag{55}$$

where Δt is the sampling interval. The expected wavelet power spectrum is:

$$\mathbb{E}[|W_x(s,\tau)|^2] = \frac{\sigma^2 P_{\mathrm{AR(1)}}(1/s)}{2}. \tag{56}$$

The significance level is determined by generating M surrogate pairs $(x^{(m)}, y^{(m)})$ and computing:

$$p(s,\tau) = \frac{1}{M}\sum_{m=1}^{M} \mathbb{I}[R^2_{\mathrm{surr}^{(m)}}(s,\tau) > R^2_{\mathrm{obs}}(s,\tau)], \tag{57}$$

where $\mathbb{I}[\cdot]$ is the indicator function.

The cone of influence accounts for edge effects where the wavelet extends beyond the data boundaries. For a time series of length T, the COI at each edge is:

$$\mathrm{COI}(t) = \frac{\sqrt{2}s_{\max}}{\psi_0}, \tag{58}$$

where $\psi_0 = \pi^{1/4}$ for the Morlet wavelet. Inside the COI, the wavelet transform is computed with zero-padding, introducing artifacts. The e-folding time for edge effects is:

$$\tau_e(s) = \sqrt{2}s. \tag{59}$$

Phase relationships provide crucial dynamical information. The relative phase:

$$\Delta\phi_{xy}(s,\tau) = \phi_y(s,\tau) - \phi_x(s,\tau), \tag{60}$$

indicates lead-lag relationships. In the complex plane representation:

$$W_{xy}(s,\tau) = |W_{xy}(s,\tau)|[\cos(\Delta\phi_{xy}) + i\sin(\Delta\phi_{xy})]. \tag{61}$$

For physical interpretation:

- $\Delta\phi_{xy} \in (-\pi/2, \pi/2)$: x leads y
- $\Delta\phi_{xy} \in (\pi/2, \pi) \cup (-\pi, -\pi/2)$: y leads x
- $|\Delta\phi_{xy}| < \pi/4$: approximately in-phase
- $|\Delta\phi_{xy} - \pi| < \pi/4$: approximately anti-phase

The instantaneous time lag is:

$$\Delta t(s,\tau) = \frac{s\Delta\phi_{xy}(s,\tau)}{2\pi}. \tag{62}$$

The global wavelet coherence spectrum:

$$\overline{R^2}(s) = \frac{1}{N_{\mathrm{valid}}}\sum_{\tau\notin\mathrm{COI}} R^2(s,\tau), \tag{63}$$

where N_{valid} is the number of points outside the COI, reveals dominant periods of coherent variability.

The scale-averaged wavelet coherence over a band $[s_1, s_2]$:

$$\overline{R^2}_{\text{scale}}(\tau) = \frac{\delta t}{C_\delta} \sum_{j=j_1}^{j_2} \frac{R^2(s_j, \tau)}{s_j}, \tag{64}$$

where $C_\delta = 0.776$ for the Morlet wavelet with $\omega_0 = 6$, provides a time series of band-integrated coherence.

The analysis was implemented using MATLAB® R2023b wavelet toolbox. The `wcoherence` function implements equations (37) through (52) with optimized algorithms. Prior to analysis, time series were standardized:

$$\tilde{x}(t) = \frac{x(t) - \mu_x}{\sigma_x}, \tag{65}$$

where μ_x and σ_x are the mean and standard deviation, ensuring comparable power across different transport components.

The wavelet coherence analysis was applied specifically to ocean transport pathways with consensus scores ≥ 2 from the causality analysis, providing time-frequency decomposition of established causal relationships. This approach reveals: (1) temporal evolution of coupling strength, (2) scale-dependent phase relationships, (3) identification of transient versus persistent coherence, and (4) dominant periods of ocean teleconnections.

3 Results

3.1 Descriptive Statistics of Ocean Volume Transport

The descriptive statistical analysis reveals distinct distributional characteristics across the three major ocean circulation systems examined in this study (Fig. 3). For the ITF components, ITF-G exhibits a mean transport of 5.996 Sv with a standard deviation of 6.034 Sv, yielding the highest coefficient of variation (100.65%) among the ITF components. The distribution shows near-symmetric properties with skewness of 0.102 and slightly negative kurtosis (-0.216). The robust statistics indicate a median of 5.958 Sv and median absolute deviation (MAD) of 4.060 Sv. Extreme values range from -9.657 Sv (April 2010) to 22.330 Sv (September 2001), with the 5th-95th percentile range spanning -3.968 to 16.066 Sv. ITF-T demonstrates a mean transport of 5.508 Sv with lower variability (SD = 5.109 Sv, CV = 92.76%) compared to ITF-G. The distribution exhibits slight negative skewness (-0.124) and light-tailed characteristics (kurtosis = -0.515). The median value of 5.627 Sv closely approximates the mean, with trimmed means at 10% and 20% levels (5.614 Sv and 5.711 Sv, respectively) indicating minimal influence from outliers. The transport ranges from -6.977 Sv (April 1992) to 20.547 Sv (July 2000). ITF-S shows the smallest absolute transport values but the highest relative variability (CV = 118.02%) among all components. The mean transport is 1.666 Sv with a standard deviation of 1.966 Sv. The distribution displays moderate negative skewness (-0.569), indicating a left-skewed pattern. The interquartile range of 2.546 Sv and the difference between median (2.009 Sv) and mean values further confirm this asymmetry. Transport values range from -4.775 Sv (March 2007) to 5.872 Sv (August 2008).

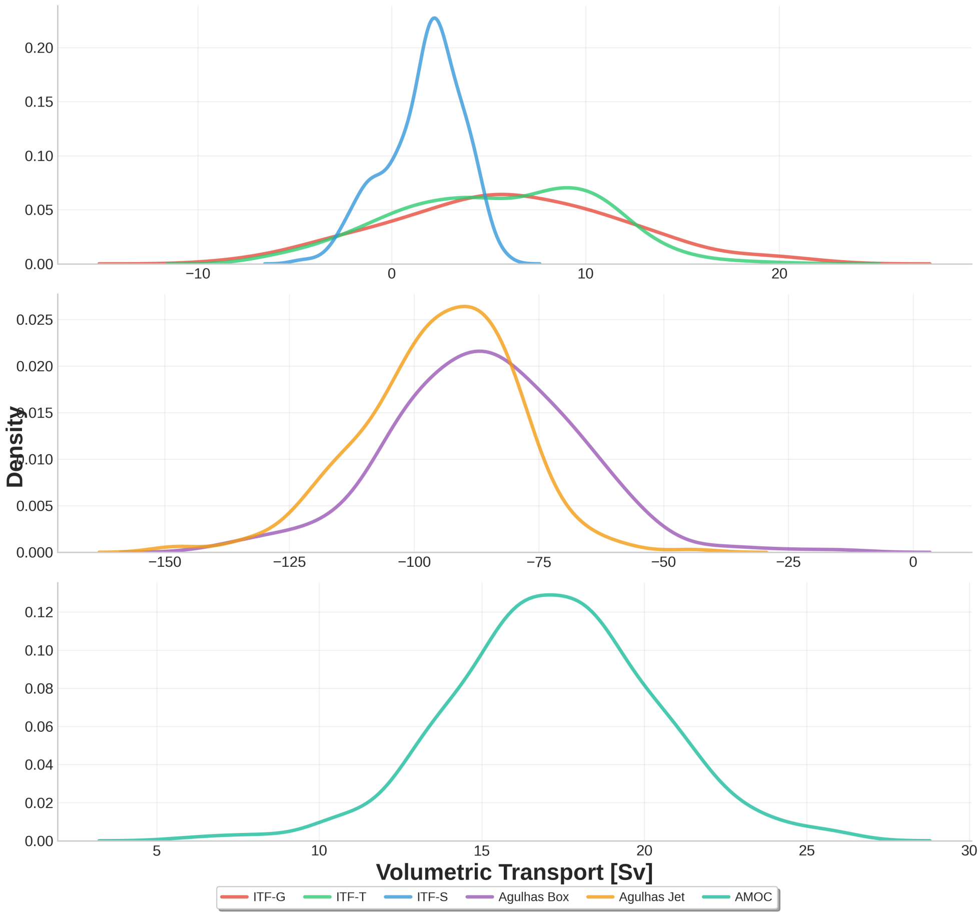

Fig. 3 Kernel density estimation (KDE) distributions of oceanic volume transport for all analyzed components. Top panel: ITF components showing ITF-G (red), ITF-T (green), and ITF-S (blue). Middle panel: Agulhas Current transports displaying Agulhas Box (purple) and Agulhas Jet (orange). Bottom panel: Atlantic Meridional Overturning Circulation (AMOC, cyan). The distributions illustrate the probability density of transport values, with ITF and AMOC showing positive transport values and Agulhas Current exhibiting negative values indicative of southwestward flow.

The AMOC demonstrates the most stable transport characteristics among all systems, with a mean of 17.182 Sv and the lowest coefficient of variation (18.08%). The distribution exhibits near-symmetric properties (skewness = -0.122) with moderate positive kurtosis (0.563), indicating heavy-tailed behavior. The standard deviation of 3.107 Sv and MAD of 1.887 Sv reflect relatively low variability. Transport values range from 6.078 Sv (March 2013) to 25.938 Sv (October 1995), with the 5th-95th percentile range spanning 12.495 to 22.052 Sv.

The comparative analysis of robust versus classical statistics reveals consistent patterns across all transport components. Trimmed means at 10% and 20% levels show minimal deviation from arithmetic means (typically less than 2%), suggesting limited influence from extreme values despite the presence of outliers in several time series. The MAD values are consistently lower than standard deviations by factors ranging from 1.49 (ITF-S) to 1.65 (AMOC), reflecting the robust estimator's resistance to outliers. Interquartile ranges provide additional outlier-resistant measures of spread, with values of 8.102 Sv (ITF-G), 7.779 Sv (ITF-T), 2.546 Sv (ITF-S), 24.808 Sv (Agulhas Box), 19.482 Sv (Agulhas Jet), and 3.753 Sv (AMOC).

3.2 Annual Cycle Characteristics

Seasonal patterns of oceanic volume transport reveal pronounced variability across different current systems, with distinct timing and magnitude of seasonal extrema (Fig. 4). The ITF components display strong seasonal cycles with considerable variation in their timing and amplitude. ITF-G reaches its peak transport of 13.017 Sv in September, while its minimum occurs in April at -0.257 Sv, resulting in a seasonal amplitude of 13.274 Sv. The annual mean transport stands at 5.996 Sv, with seasonal variations accounting for 74.09% of the mean (coefficient of variation). ITF-T exhibits the largest seasonal amplitude among the ITF components at 14.114 Sv. Maximum transport occurs in July (11.722 Sv), with the minimum in April (-2.393 Sv). Despite similar annual mean transport to ITF-G (5.508 Sv), ITF-T shows stronger seasonal modulation with a coefficient of variation of 83.29%. ITF-S demonstrates the most pronounced relative seasonal variability, with a coefficient of variation reaching 103.48%. Although its absolute seasonal amplitude is smaller (5.525 Sv), this represents a substantial fraction of its annual mean transport of 1.666 Sv. Peak transport occurs in September (4.028 Sv), while the minimum is observed in February (-1.497 Sv).

The Agulhas Current system shows consistent seasonal patterns between its two measurement approaches, though with different magnitudes. Agulhas Box transport reaches its weakest southwestward flow of -75.268 Sv in July and strongest flow of -97.927 Sv in March, yielding a seasonal amplitude of 22.659 Sv. The annual mean transport is -85.982 Sv, with relatively modest seasonal variation (coefficient of variation of -9.22%). Agulhas Jet measurements follow a similar seasonal pattern but with stronger mean flow and slightly reduced amplitude. The weakest southwestward transport occurs at -85.879 Sv in July, while the strongest flow of -103.185 Sv is observed in March, producing a seasonal amplitude of 17.306 Sv. The annual mean of -95.097 Sv combined with this amplitude results in a coefficient of variation of -5.71%, the smallest relative seasonal variation among the ITF and Agulhas components.

The AMOC exhibits the most stable seasonal behavior of all systems examined. Transport varies from a minimum of 15.195 Sv in April to a maximum of 18.722 Sv in November, creating a modest seasonal amplitude of 3.528 Sv. With an annual mean of 17.182 Sv, this translates to a coefficient of variation of just 7.07%, indicating relatively weak seasonal modulation compared to other current systems.

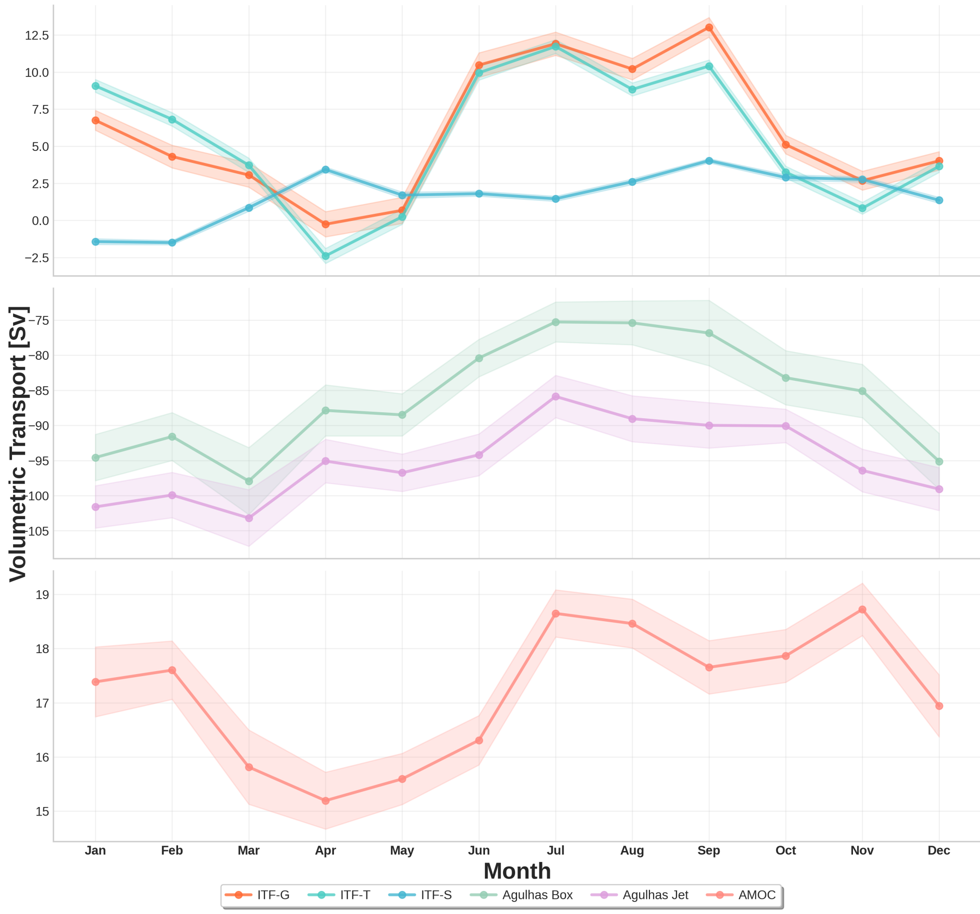

Fig. 4 Monthly climatological mean volume transport for all ocean current components. Top panel: ITF components (ITF-G in orange, ITF-T in teal, ITF-S in blue). Middle panel: Agulhas Current transports (Agulhas Box in green, Agulhas Jet in purple). Bottom panel: Atlantic Meridional Overturning Circulation (AMOC in red). Shaded areas represent standard errors around the monthly means. All values are in Sv.

Across all transport components, April emerges as a common month for minimum values, appearing in the seasonal minima for ITF-G, ITF-T, and AMOC. For the Agulhas components, March marks the period of strongest southwestward flow, while July shows the weakest flow. September represents peak transport for ITF-G and ITF-S. The timing of these extrema, combined with the varying amplitudes and coefficients of variation, highlights the diverse seasonal characteristics inherent to each ocean circulation system. Standard errors around monthly means, visualized as shaded regions in Fig. 4, provide measures of interannual variability within each calendar month. These uncertainties vary both seasonally and between transport components, with generally larger standard errors observed during months of maximum transport, particularly evident in the ITF components.

3.3 Long-term Trends

Analysis of multi-decadal transport trends using the Theil-Sen estimator reveals significant changes in half of the examined current systems, with the Mann-Kendall test confirming statistical significance at the $p < 0.05$ level (Fig. 5).

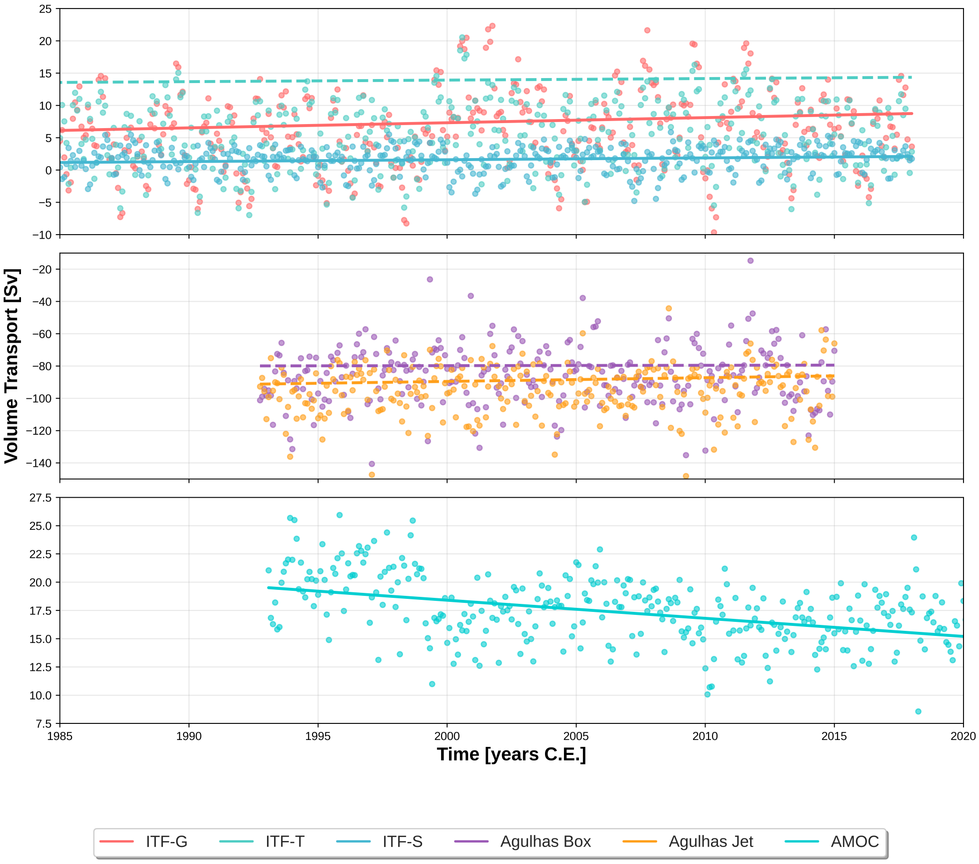

Fig. 5 Long-term trends in oceanic volume transport from 1984-2023. Top panel: ITF components (ITF-G in red, ITF-T in cyan, ITF-S in blue). Middle panel: Agulhas Current transports (Agulhas Box in purple, Agulhas Jet in orange). Bottom panel: AMOC (cyan). Individual monthly data points are shown with Theil-Sen regression trends over the available data periods. Solid lines indicate statistically significant trends (p < 0.05), dashed lines indicate non-significant trends. All transport values in Sv.

Among the ITF components, ITF-G shows the strongest upward trend at 0.079 Sv per year, equivalent to an increase of 0.79 Sv per decade over its 1984-2017 measurement period. This trend proves statistically significant ($p = 0.012$), suggesting a robust strengthening of transport through this pathway. Similarly, ITF-S exhibits a significant positive trend of 0.028 Sv per year ($p = 0.007$), corresponding to a decadal increase of 0.28 Sv. In contrast, ITF-T displays a weaker positive trend of 0.024 Sv per year that fails to reach statistical significance ($p = 0.374$), indicating considerable uncertainty in the long-term behavior of this component.

The Agulhas Current system presents no statistically significant trends during the 1993-2015 observation period. Agulhas Box measurements show a minimal positive trend of 0.021 Sv per year ($p = 0.876$), which would represent a slight weakening of the southwestward flow if real, though the high p-value suggests this apparent trend could easily arise from natural variability alone. The Agulhas Jet data indicates a more substantial positive trend of 0.229 Sv per year, implying a potential weakening of 2.29 Sv per decade in southwestward transport. However, this trend also lacks statistical significance ($p = 0.136$), preventing firm conclusions about long-term changes in the Agulhas system.

The AMOC stands out as exhibiting the most pronounced and statistically robust trend among all systems analyzed. The negative trend of -0.161 Sv per year is highly significant ($p < 0.0001$), indicating a decline of 1.61 Sv per decade over the 1993-2024 measurement period. This represents the only significant negative trend detected across all transport components and suggests a substantial weakening of the Atlantic overturning circulation during recent decades.

The analysis encompasses different time periods for each current system, reflecting data availability constraints. The ITF components provide the longest records (1984-2017), while the Agulhas measurements cover a shorter span (1993-2015). The AMOC data extends most recently, reaching through 2023. Despite these varying temporal coverages, all trend analyses are plotted on a consistent 1984-2023 axis to facilitate visual comparison.

Overall, three of the six transport time series demonstrate statistically significant long-term trends: strengthening flows through ITF-G and ITF-S, and weakening circulation in the AMOC. The remaining components show trends that, while potentially meaningful in magnitude, cannot be distinguished from natural variability at the 95% confidence level. The Theil-Sen method's resistance to outliers provides robust trend estimates even in the presence of extreme events visible in several time series, particularly the substantial variability evident in the Agulhas Current measurements.

3.4 Statistical Causal Relationships Between Current Systems

The statitical causality analysis reveals multiple significant connections linking the Indonesian Throughflow, Agulhas system, and Atlantic Meridional Overturning Circulation across 264 months of observations (January 1993 to December 2014). Among the eleven pathways tested, four demonstrate robust causal relationships with consensus support from at least two independent methods (Table 1).

The geostrophic component of the ITF emerges as a key driver of Agulhas variability through two distinct pathways. The ITF-G to Agulhas Box connection exhibits significant negative correlation (r = -0.280, $p < 0.01$) with an 18-month lead time, accompanied by moderate nonlinear coupling ($\rho = 0.237$, $p < 0.05$). In contrast, the ITF-G influence on Agulhas Jet transport occurs almost instantaneously, showing strong positive correlation (r = 0.264, $p < 0.01$) at just one month lag and the highest CCM strength among all pathways ($\rho = 0.302$, $p < 0.01$).

Temperature and salinity components of the ITF also display significant causal influences on Agulhas Box transport, though with markedly different temporal characteristics. The temperature signal shows immediate impact with zero lag (r = 0.223, $p < 0.05$) and strong nonlinear causality ($\rho = 0.241$, $p < 0.01$). Meanwhile, the salinity component requires 12 months to manifest its influence, producing the highest linear correlation among dominant pathways (r = 0.265, $p < 0.05$) alongside significant CCM detection ($\rho = 0.193$, $p < 0.05$).

Table 1 Summary of causality analysis for ocean transport pathways. MCC values with optimal lag, CCM strength, TE, and consensus scores are shown. Bold entries indicate dominant pathways with consensus ≥ 2.

Pathway	**MCC (r)**	**Lag (months)**	**CCM (ρ)**	**TE (bits)**	**Consensus Score**
ITF-G → Agulhas Box	-0.280**	-18	0.237*	0.182	2
ITF-G → Agulhas Jet	0.264**	-1	0.302**	0.180	2
ITF-T → Agulhas Box	0.223*	0	0.241**	0.168	2
ITF-S → Agulhas Box	0.265*	-12	0.193*	0.173	2
ITF-T → Agulhas Jet	0.196	0	0.186	0.192	0
ITF-S → Agulhas Jet	0.145	-18	0.124	0.162	0
Agulhas Box → AMOC	0.113	0	0.152	0.171	0
Agulhas Jet → AMOC	0.178	-6	0.146	0.175	0
ITF-G → AMOC	0.142	0	0.167	0.185	0
ITF-T → AMOC	0.097	-12	0.114	0.168	0
ITF-S → AMOC	0.156	-18	0.138	0.177	0

*$p < 0.05$, **$p < 0.01$ based on block bootstrap testing (500-1000 surrogates)

TE values remain relatively uniform across all pathways, ranging from 0.162 to 0.192 normalized bits, with the ITF-T to Agulhas Jet pathway showing the highest information flow despite lacking statistical significance. Notably, no significant causal relationships emerge between the Agulhas system and AMOC in either direction, with all consensus scores remaining at zero. Direct connections from ITF components to AMOC similarly fail to achieve significance in any metric, despite moderate TE values that suggest some information transfer may occur.

The temporal structure of the statistical causal relationships varies considerably among pathways. Lead times range from near-instantaneous coupling (0-1 months) for temperature and jet-related pathways to extended propagation periods (12-18 months) for salinity and box transport connections. This diversity in lag times persists even when comparing different ITF components affecting the same Agulhas metric, suggesting distinct physical mechanisms may govern each interaction. The block bootstrap procedure confirms these patterns remain robust when accounting for the inherent autocorrelation structure present in monthly ocean transport time series.

3.5 Wavelet Coherence of Significant Causal Pathways

Wavelet coherence analysis was performed on the four ocean transport pathways identified as statistically significant in the causality analysis (consensus score ≥ 2). The analysis encompasses 268 data points spanning 22.25 years (1992.67 to 2014.92) with a monthly sampling interval of 0.085 years. Figure 6 presents the wavelet coherence scalograms for the four pathways, with periods ranging from 0.2 to 8.3 years.

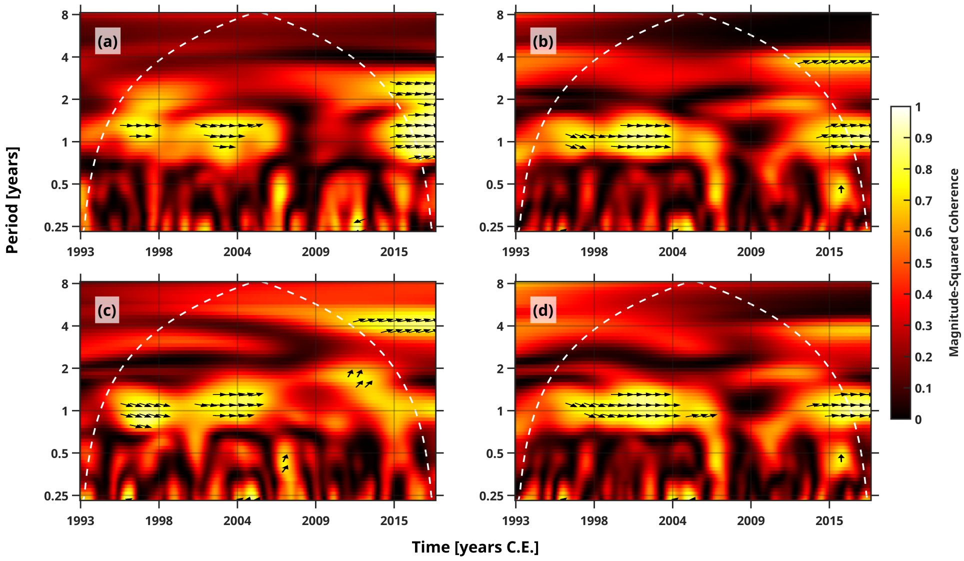

Fig. 6 Wavelet coherence between ITF components and Agulhas transport metrics. (a) ITF Salinity and Agulhas Box transport. (b) ITF Temperature and Agulhas Box transport. (c) ITF Geostrophic and Agulhas Jet transport. (d) ITF Geostrophic and Agulhas Box transport. The magnitude-squared coherence is shown by the color scale (0-1), with warmer colors indicating stronger coherence. Black arrows indicate phase relationships, displayed only where coherence exceeds 0.7. Rightward arrows indicate in-phase behavior, leftward arrows indicate anti-phase relationships, and vertical arrows indicate quadrature. The white dashed lines delineate the cone of influence where edge effects become significant.

For the ITF Salinity-Agulhas Box pathway (Fig. 6a), the average coherence across all time-frequency space is 0.315, with 6.8% of the region exhibiting coherence values above 0.7. The five most dominant periods show average coherence values ranging from 0.545 to 0.599, with the strongest occurring at 1.23 years (0.599), followed by 1.16 years (0.595), 1.30 years (0.579), 1.09 years (0.574), and 1.03 years (0.545). High coherence (¿0.7) at the 1.23-year period appears during three distinct intervals: 1995.3-1997.4, 1999.7-2004.2, and 2012.1-2014.9. The average phase angle in high-coherence regions is -0.11 radians (-6.5 degrees), indicating approximately in-phase behavior.

The ITF Temperature-Agulhas Box pathway (Fig. 6b) displays an average coherence of 0.293, with 5.9% of the analyzed region showing coherence above 0.7. The dominant periods cluster around the annual cycle, with the strongest coherence at 0.97 years (0.604), followed by 1.03 years (0.603), 0.92 years (0.596), 1.09 years (0.595), and 1.16 years (0.577). High coherence at the 0.97-year period occurs during 1995.9-2002.5, briefly during 2004.4-2004.6, and again during 2012.0-2014.9. The average phase angle of 0.09 radians (5.3 degrees) in high-coherence regions indicates approximately in-phase relationships.

The ITF Geostrophic-Agulhas Jet pathway (Fig. 6c) exhibits an average coherence of 0.348, with 6.4% of the time-frequency space exceeding the 0.7 coherence threshold. The dominant periods show similar annual-scale preferences: 1.09 years (0.600), 1.03 years (0.599), 0.97 years (0.590), 1.16 years (0.590), and 0.92 years (0.575). High coherence at the 1.09-year period manifests during two main intervals: 1995.4-1998.2 and 1999.8-2004.1. The average phase angle in high-coherence regions is 0.18 radians (10.4 degrees), remaining within the in-phase classification.

The ITF Geostrophic-Agulhas Box pathway (Fig. 6d) shows an average coherence of 0.317, with 6.2% of the analyzed domain displaying coherence above 0.7. The dominant periods exhibit the strongest coherence values among all pathways: 0.97 years (0.616), 0.92 years (0.613), 1.03 years (0.612), 1.09 years (0.600), and 0.87 years (0.598). High coherence at the 0.97-year period persists through extended intervals: 1996.2-2004.8 and 2011.7-2014.9. The average phase angle of 0.03 radians (1.6 degrees) represents the smallest phase offset among all analyzed pathways.

Cross-panel comparison reveals five periods that maintain coherence above 0.5 across all four pathways. These common periods center on the annual cycle: 1.09 years (average coherence 0.592), 1.03 years (0.590), 1.16 years (0.586), 0.97 years (0.581), and 1.23 years (0.567). The concentration of dominant periods between 0.87 and 1.30 years across all pathways indicates systematic annual-scale coupling between ITF components and Agulhas transport variability.

All pathways display approximately in-phase behavior in their high-coherence regions, with phase angles ranging from 1.6 to 10.4 degrees. The temporal distribution of high coherence shows notable clustering during three periods: the mid-to-late 1990s (approximately 1995-1998), an extended period from the late 1990s through early 2000s (approximately 1999-2004), and a recent period from 2012 to the end of the record in 2014. These intervals of enhanced coherence appear consistently across multiple pathways, though with slight variations in exact timing and duration.

4 Discussion

The analysis of multi-decadal ocean transport time series reveals significant trends and teleconnections within the global circulation system, with important implications for understanding climate variability and change. Our findings demonstrate strengthening of the ITF, weakening of the AMOC, and robust statistical causal connections between the ITF and Agulhas Current system, though notably without direct linkages to the AMOC.

The observed strengthening trends in ITF-G (0.79 Sv per decade) and ITF-S (0.28 Sv per decade) align remarkably well with recent observational evidence. Hu and Sprintall (2017) reported ITF strengthening linked to rainfall intensification over the Maritime Continent, while Feng et al. (2018) documented a centennial strengthening trend of approximately 1 Sv per decade. Our results fall within this range, though slightly lower than the 1.33 Sv per decade reported for more recent periods. The dominance of the geostrophic component in driving the overall trend suggests that large-scale pressure gradient changes, rather than local wind forcing, control the long-term ITF evolution. This finding has profound implications for understanding how regional climate changes translate into basin-scale ocean circulation adjustments.

The strong seasonal variability observed across all ITF components, with peak transports occurring during the Southeast Monsoon period, corroborates the established understanding of monsoonal control on ITF variability (Gordon 2005). What makes our findings particularly striking is the coefficient of variation exceeding 100% for ITF-G and ITF-S, indicating that interannual variability rivals the mean transport. This extreme variability, consistent with strong ENSO modulation documented by Sprintall et al. (2009), suggests that detecting long-term trends requires careful consideration of natural climate oscillations superimposed on anthropogenic signals.

Turning to the Atlantic sector, the highly significant weakening trend of -1.61 Sv per decade in the AMOC represents one of the most robust findings in this study. This decline exceeds the -1.0 Sv per decade reported from the RAPID array for 2004-2023 (McCarthy et al. 2025), raising questions about either an acceleration of the weakening or methodological differences between reanalysis products and direct observations. Caesar et al. (2018) identified a 15% weakening since the mid-20th century using fingerprint analysis, which translates to approximately 2-3 Sv total decline—a figure consistent with our findings when extrapolated over similar timescales. The relatively low coefficient of variation for AMOC compared to other transport components indicates a more stable baseline state, making the detection of long-term trends particularly robust. This stability, combined with the high statistical significance of the trend, provides compelling evidence for systematic AMOC weakening during the recent warming period.

The identification of four dominant causal pathways from ITF components to Agulhas transport reveals complex, scale-dependent teleconnections operating through the Indian Ocean. The varying lag times—from instantaneous coupling for ITF-T to Agulhas Box, to 18-month lags for ITF-G to Agulhas Box—suggest multiple physical mechanisms at play. While Durgadoo et al. (2017) demonstrated that ITF waters require 10-20 years to reach the Agulhas retroflection region via the classical oceanic pathway, our shorter lag times likely reflect faster, upper-ocean pathways or atmospheric teleconnections that modify both systems coherently. The opposite signs of correlation between ITF-G and the two Agulhas metrics reveal an intriguing dynamic: increased ITF transport may enhance the Agulhas Current core velocity while broadening the current, thereby reducing the integrated transport across the fixed Box section. This interpretation aligns with theoretical predictions by Biastoch et al. (2009) who showed that enhanced ITF can modify the Agulhas Current structure through changes in Indian Ocean thermocline depth.

Perhaps most intriguing is the complete absence of statistically significant causal connections between either ITF or Agulhas components and the AMOC. This null result challenges simple conceptual models of a continuous global conveyor belt where enhanced ITF would directly influence Atlantic overturning. Several factors may explain this unexpected finding. The oceanic pathway from the Indian to Atlantic Ocean involves complex transformations, with Biastoch et al. (2008) demonstrating that Agulhas leakage waters undergo substantial modification in the South Atlantic through mixing and air-sea interaction that obscures source water properties. Additionally, Weijer et al. (2019) showed that AMOC variability is dominated by high-latitude processes in the North Atlantic, potentially overwhelming far-field influences from the Indo-Pacific sector.

This lack of direct connections does not preclude indirect influences operating through atmospheric teleconnections. Recent work by McGregor et al. (2014) demonstrated that Atlantic warming can influence Pacific climate through atmospheric bridges, suggesting similar processes might operate in reverse. Furthermore, Sun and Thompson (2020) found centennial-scale connections between ITF and AMOC in model simulations, indicating that our 22-year analysis period may be insufficient to detect these longer-timescale relationships. The ocean's memory at these timescales extends far beyond our observational window, highlighting the critical need for sustained observations and paleoceanographic reconstructions.

The concentration of significant wavelet coherence at periods between 0.87-1.30 years across all ITF-Agulhas pathways reveals a fundamental annual-scale coupling mechanism. This coherence likely reflects the monsoon system's pervasive influence on both the ITF and Indian Ocean circulation (Schott et al. 2009). The approximately in-phase relationships, with phase angles ranging from merely 1.6 to 10.4 degrees, suggest near-simultaneous responses to common forcing. This timing is more consistent with basin-scale atmospheric forcing than with slow oceanic wave propagation, which would introduce substantial phase lags. The temporal clustering of high coherence during specific periods—1995-1998, 1999-2004, and 2012-2014—coincides with major climate events including the 1997-98 El Niño, the early 2000s Indo-Pacific regime shift, and the 2014-16 warming event. This episodic coherence suggests that the strength of ITF-Agulhas coupling varies dramatically with the background climate state, potentially explaining some of the complexity in the causal relationships we observe.

The multi-method causality approach employed here provides robust detection of ocean teleconnections while accounting for both linear and nonlinear relationships. By combining MCC, CCM, and TE, we capture different aspects of dynamical coupling that single methods might miss. The consensus requirement reduces false positive rates inherent in multiple testing, while the application of block bootstrap methods preserves the autocorrelation structure critical for oceanographic time series (Sugihara et al. 2012). However, several limitations warrant consideration. The varying temporal coverage of different datasets introduces potential biases in trend estimates and limits the overlap period for causality analysis. The monthly resolution, while appropriate for detecting seasonal to interannual relationships, may miss higher-frequency coupling mechanisms that could reveal additional dynamical pathways. Additionally, the use of different measurement approaches—geostrophic calculations for ITF, satellite altimetry for Agulhas, and reanalysis for AMOC—introduces methodological uncertainties that complicate inter-basin comparisons.

Our results support a view of the global ocean circulation as a complex, multi-scale system rather than a simple conveyor belt. The simultaneous strengthening of ITF and weakening of AMOC, yet their apparent dynamical decoupling on the timescales analyzed, suggests that regional processes dominate over global-scale connections. Enhanced rainfall and wind forcing in the Maritime Continent drive ITF changes (Hu and Sprintall 2017), while weakened deep convection in the North Atlantic controls AMOC variability (Thornalley et al. 2018). These regional drivers appear to overwhelm any direct inter-basin coupling, at least on the timescales accessible to current observations.

The robust ITF-Agulhas connections indicate that changes in Pacific-Indian Ocean exchange do propagate into the South Atlantic gateway, potentially preconditioning the Atlantic for longer-term changes. The 12-18 month lag times for some pathways suggest that ITF variations could provide predictability for Agulhas transport and potentially South Atlantic climate. This predictability, if properly harnessed, could improve seasonal to interannual forecasts for regions influenced by Agulhas leakage, including South Atlantic hurricane development and Benguela upwelling dynamics. As the climate continues to warm and these circulation systems evolve, monitoring these critical ocean gateways becomes increasingly important for understanding and predicting changes in global ocean circulation and regional climate impacts. Future work should focus on extending these time series to detect longer-period variability, investigating atmospheric teleconnections between ocean basins, and developing process-based understanding of the mechanisms underlying the statistical relationships identified here.

5 Conclusions and Future Work

This comprehensive statistical analysis of ocean transport variability reveals fundamental characteristics of the global ocean circulation system and its response to contemporary climate forcing. Through systematic application of non-parametric trend analysis, multi-method causality testing, and wavelet coherence examination, we identified contrasting behaviors across ocean basins: significant strengthening of the ITF, robust weakening of the AMOC, and stable but highly variable Agulhas Current transport. The causality analysis uncovered multiple statistically significant pathways linking ITF components to Agulhas transport variability, yet notably absent were any direct connections to the AMOC, challenging traditional paradigms of a tightly coupled global conveyor belt. The dominant annual-scale coherence in ITF-Agulhas coupling, with episodic strengthening during major climate events, indicates that monsoon-driven atmospheric forcing provides the primary teleconnection mechanism rather than slow oceanic advection. These findings support a paradigm wherein regional forcing mechanisms—enhanced Maritime Continent rainfall for ITF and weakened North Atlantic convection for AMOC—dominate over global-scale connectivity on observable timescales.

Future investigations should expand this statistical framework through comprehensive spatio-temporal climate field analysis to identify coherent patterns of variability across ocean basins and elucidate whether the identified connections manifest as propagating subsurface anomalies or atmospheric forcing patterns. Process-oriented modeling experiments with controlled perturbations could distinguish between oceanic and atmospheric teleconnection pathways, while paleoclimate analog studies, particularly of the mid-Pliocene Warm Period and Heinrich events, may reveal precedents for the simultaneous ITF strengthening and AMOC weakening observed in the contemporary ocean. Extended temporal analyses combining proxy reconstructions and long model simulations are essential to detect potential centennial-scale inter-basin connections beyond our current observational window. As anthropogenic forcing continues to perturb the climate system, understanding both the regional responses and evolving connectivity of ocean currents becomes increasingly critical for projecting future climate trajectories and informing adaptation strategies, with the framework developed here providing a robust approach for monitoring these changes as they unfold.

Author Contributions. **S.H.S.H.**: Conceptualization; Data curation; Formal analysis; Methodology; Software; Visualization; Writing – original draft. **K.E.P.H.**: Conceptualization; Software; Visualization; Writing – review & editing. **I.P.A.**: Conceptualization; Supervision; Writing – review & editing. **S.Y.C.**: Supervision; Writing – review & editing. All authors reviewed and approved the final version of the manuscript.

Funding. This study was supported by the Dean's Distinguished Fellowship from the College of Natural and Agricultural Sciences (CNAS) at the University of California, Riverside in 2023.

Data Availability. The following datasets were utilized in this study:

- Agulhas Current data: https://beal-agulhas.earth.miami.edu/data-and-products/index.html.
- Atlantic Meridional Overturning Circulation (AMOC) data: https://doi.org/10.48670/moi-00232.
- Indonesian Throughflow (ITF) data: http://doi.org/10.12157/IOCAS.20221214.001.

All derived datasets, analytical code, visualization scripts, statistical outputs, and figure generation routines are publicly available in the GitHub repository at https://github.com/sandyherho/amocITFAghulasTimeSeries, released under the WTFPL (Do What The F*ck You Want To Public License).

Declarations

Conflict of interest. The authors declare there is no conflict.

Competing interests. Authors do not have any competing financial interest to declare.

Ethical Approval. Not Applicable

References

Barker DM, Huang W, Guo YR, Bourgeois A, Xiao Q. A Three-Dimensional Variational Data Assimilation System for MM5: Implementation and Initial Results. Mon Weather Rev. 2004;132(4):897–914. https://doi.org/10.1175/1520-0493(2004)132⟨0897:ATVDAS⟩2.0.CO;2.

Beal LM, Elipot S. Broadening not strengthening of the Agulhas Current since the early 1990s. Nature. 2016;540(7634):570–573. https://doi.org/10.1038/nature19853.

Biastoch A, Böning CW, Lutjeharms JRE. Agulhas leakage dynamics affects decadal variability in Atlantic overturning circulation. Nature. 2008;456:489–492. https://doi.org/10.1038/nature07426.

Biastoch A, Böning CW, Schwarzkopf FU, Lutjeharms JRE. Increase in Agulhas leakage due to poleward shift of Southern Hemisphere westerlies. Nature. 2009;462:495–498. https://doi.org/10.1038/nature08519.

Boers N. Observation-based early-warning signals for a collapse of the Atlantic Meridional Overturning Circulation. Nat Clim Change. 2021;11(8):680–688. https://doi.org/10.1038/s41558-021-01097-4.

Bretherton CS, Smith C, Wallace JM. An Intercomparison of Methods for Finding Coupled Patterns in Climate Data. J Clim. 1992;5(6):541–560. https://doi.org/10.1175/1520-0442(1992)005⟨0541:AIOMFF⟩2.0.CO;2.

Broecker WS. Unpleasant surprises in the greenhouse? Nature. 1987;328(6126):123–126. https://doi.org/10.1038/328123a0.

Broecker WS. The great ocean conveyor. Oceanography. 1991;4(2):79–89. https://doi.org/10.5670/oceanog.1991.07.

Caesar L, McCarthy GD, Thornalley DJR, Cahill N, Rahmstorf S. Current Atlantic Meridional Overturning Circulation weakest in last millennium. Nat Geosci. 2021;14:118–120. https://doi.org/10.1038/s41561-021-00699-z.

Caesar L, Rahmstorf S, Robinson A, Feulner G, Saba V. Observed fingerprint of a weakening Atlantic Ocean overturning circulation. Nature. 2018;556:191–196. https://doi.org/10.1038/s41586-018-0006-5.

Cheng L, Trenberth KE, Gruber N, Abraham JP, Fasullo JT, Li G, et al. Improved Estimates of Changes in Upper Ocean Salinity and the Hydrological Cycle. J Clim. 2020;33(23):10357–10381. https://doi.org/10.1175/JCLI-D-20-0366.1.

Cheng L, Zhu J, Cowley R, Boyer T, Wijffels S. Time, Probe Type, and Temperature Variable Bias Corrections to Historical Expendable Bathythermograph Observations. J Atmos Ocean Technol. 2014;31(8):1793–1825. https://doi.org/10.1175/JTECH-D-13-00197.1.

Dee DP, Uppala SM, Simmons AJ, Berrisford P, Poli P, Kobayashi S, et al. The ERA-Interim reanalysis: configuration and performance of the data assimilation system. Q J R Meteorol Soc. 2011;137(656):553–597. https://doi.org/10.1002/qj.828.

Ditlevsen P, Ditlevsen S. Warning of a forthcoming collapse of the Atlantic meridional overturning circulation. Nat Commun. 2023;14(1):4254. https://doi.org/10.1038/s41467-023-39810-w.

Dobricic S, Pinardi N. An oceanographic three-dimensional variational data assimilation scheme. Oce Mod. 2008;22(3):89–105. https://doi.org/10.1016/j.ocemod.2008.01.004.

Duchez A, Courtois P, Harris E, Josey SA, Kanzow T, Marsh R, et al. Potential for seasonal prediction of Atlantic sea surface temperatures using the RAPID array at 26°N. Clim Dyn. 2016;46:3351–3370. https://doi.org/10.1007/s00382-015-2918-1.

Durgadoo JV, Rühs S, Biastoch A, Böning CWB. Indian Ocean sources of Agulhas leakage. J Geophys Res Oceans. 2017;122(4):3481–3499. https://doi.org/10.1002/2016JC012676.

Efron B, Tibshirani RJ. An Introduction to the Bootstrap. New York: Chapman and Hall/CRC; 1994. https://doi.org/10.1201/9780429246593.

E U Copernicus Marine Service Information (CMEMS).: Atlantic Meridional Overturning Circulation AMOC timeseries at 26N from Reanalysis. Marine Data Store (MDS); 2024. https://doi.org/10.48670/moi-00232 (Accessed on May 28, 2025).

E U Copernicus Marine Service Information (CMEMS).: Global Ocean Ensemble Physics Reanalysis. Marine Data Store (MDS); 2024. https://doi.org/10.48670/moi-00024 (Accessed on May 28, 2025).

Farge M. Wavelet Transforms and Their Applications to Turbulence. Annual Review of Fluid Mechanics. 1992;24(1):395–458. https://doi.org/10.1146/annurev.fl.24.010192.002143.

Feng M, Zhang N, Liu Q, Wijffels S. The Indonesian throughflow, its variability and centennial change. Geosci Lett. 2018;5:3. https://doi.org/10.1186/s40562-018-0102-2.

Gordon AL. Interocean exchange of thermocline water. J Geophys Res Oceans. 1986;91(C4):5037–5046. https://doi.org/10.1029/JC091iC04p05037.

Gordon AL. Oceanography of the Indonesian Seas and their throughflow. Oceanography. 2005;18(4):14–27. https://doi.org/10.5670/oceanog.2005.01.

Gouretski V, Cheng L. Correction for Systematic Errors in the Global Dataset of Temperature Profiles from Mechanical Bathythermographs. J Atmos Ocean Technol.

2020;37(5):841–855. https://doi.org/10.1175/JTECH-D-19-0205.1.

Grinsted A, Moore JC, Jevrejeva S. Application of the cross wavelet transform and wavelet coherence to geophysical time series. Nonlinear Processes in Geophysics. 2004;11(5/6):561–566. https://doi.org/10.5194/npg-11-561-2004.

Guo Y, Li Y, Cheng L, Chen G, Liu Q, Tian T, et al. An Updated Estimate of the Indonesian Throughflow Geostrophic Transport: Interannual Variability and Salinity Effect. Geophys Res Lett. 2023;50(13):e2023GL103748. https://doi.org/10.1029/2023GL103748.

Harris CR, Millman KJ, van der Walt SJ, Gommers R, Virtanen P, Cournapeau D, et al. Array programming with NumPy. Nature. 2020 09;585(7825):357–362. https://doi.org/10.1038/s41586-020-2649-2.

Hersbach H, Bell B, Berrisford P, Hirahara S, Horányi A, Muñoz-Sabater J, et al. The ERA5 global reanalysis. Q J R Meteorol Soc. 2020;146(730):1999–2049. https://doi.org/10.1002/qj.3803.

Hu S, Sprintall J. Observed strengthening of interbasin exchange via the Indonesian Seas due to rainfall intensification. Geophys Res Lett. 2017;44(3):1448–1456. https://doi.org/10.1002/2016GL072494.

Kendall MG. Rank Correlation Methods. 4 ed. London: Charles Griffin; 1975.

Kennel MB, Brown R, Abarbanel HDI. Determining embedding dimension for phase-space reconstruction using a geometrical construction. Phys Rev A. 1992;45(6):3403–3411. https://doi.org/10.1103/PhysRevA.45.3403.

Lellouche JM, Le Galloudec O, Drévillon M, Régnier C, Greiner E, Garric G, et al. Evaluation of global monitoring and forecasting systems at Mercator Océan. Ocean Sci. 2013;9(1):57–81. https://doi.org/10.5194/os-9-57-2013.

Lenton TM, Held H, Kriegler E, Hall JW, Lucht W, Rahmstorf S, et al. Tipping elements in the Earth's climate system. Proc Natl Acad Sci USA. 2008;105(6):1786–1793. https://doi.org/10.1073/pnas.0705414105.

Lutjeharms JRE, van Ballegooyen RC. The retroflection of the Agulhas Current. J Phys Oceanogr. 1988;18(11):1570–1583. https://doi.org/10.1175/1520-0485(1988)018⟨1570:TROTAC⟩2.0.CO;2.

MacLachlan C, Arribas A, Peterson KA, Maidens A, Fereday D, Scaife AA, et al. Global Seasonal forecast system version 5 (GloSea5): a high-resolution seasonal forecast system. Q J R Meteorol Soc. 2015;141(689):1072–1084. https://doi.org/10.1002/qj.2396.

Madec G, NEMO team.: NEMO ocean engine – version 3.6 stable. Note du Pole de modélisation, Institut Pierre-Simon Laplace (IPSL) No. 27; 2015. https://epic.awi.de/id/eprint/39698/1/NEMO_book_v6039.pdf (Accessed on May 28, 2025).

Mann HB. Nonparametric Tests Against Trend. Econometrica. 1945;13(3):245–259. https://doi.org/10.2307/1907187.

McCarthy GD, et al. Signal and Noise in the Atlantic Meridional Overturning Circulation at 26°N. Geophys Res Lett. 2025;52:e2025GL115055. https://doi.org/10.1029/2025GL115055.

McGregor S, Timmermann A, Stuecker MF, England MH, Merrifield M, Jin FF, et al. Recent Walker circulation strengthening and Pacific cooling amplified by Atlantic warming. Nat Clim Change. 2014;4:888–892. https://doi.org/10.1038/nclimate2330.

McKinney W. pandas: a foundational Python library for data analysis and statistics. Python for High Performance and Scientific Computing. 2011;14(9):1–9. https://docslib.org/doc/4231522/a-foundational-python-library-for-data-analysis-and-statistics.

Moat B, Smeed D, Rayner D, Johns W, Smith R, Volkov D, et al.: Atlantic meridional overturning circulation observed by the RAPID-MOCHA-WBTS (RAPID-Meridional Overturning Circulation and Heatflux Array-Western Boundary Time Series) array at 26N from 2004 to 2023 (v2023.1a). NERC EDS British Oceanographic Data Centre NOC; 2025. https://doi.org/10.5285/33826d6e-801c-b0a7-e063-7086abc0b9db (Accesed on May 27, 2025).

Paluš M, Vejmelka M. Directionality of coupling from bivariate time series: How to avoid false causalities and missed connections. Phys Rev E. 2007;75(5):056211. https://doi.org/10.1103/PhysRevE.75.056211.

Pedregosa F, Varoquaux G, Gramfort A, Michel V, Thirion B, Grisel O, et al. Scikit-learn: Machine learning in Python. J Mach Learn Res. 2011;12:2825–2830. https://www.jmlr.org/papers/volume12/pedregosa11a/pedregosa11a.pdf.

Pham DT, Verron J, Roubaud MC. A singular evolutive extended Kalman filter for data assimilation in oceanography. J Mar Syst. 1998;16(3-4):323–340. https://doi.org/10.1016/S0924-7963(97)00109-7.

Politis DN, Romano JP. The stationary bootstrap. J Am Stat Assoc. 1994;89(428):1303–1313. https://doi.org/10.1080/01621459.1994.10476870.

Rahmstorf S. Bifurcations of the Atlantic thermohaline circulation in response to changes in the hydrological cycle. Nature. 1995;378(6553):145–149. https://doi.org/10.1038/378145a0.

Rayner NA, Brohan P, Parker DE, Folland CK, Kennedy JJ, Vanicek M, et al. Improved Analyses of Changes and Uncertainties in Sea Surface Temperature Measured In Situ Since the Mid-Nineteenth Century: The HadSST2 Dataset. J Clim. 2006;19(3):446–469. https://doi.org/10.1175/JCLI3637.1.

Rousset C, Vancoppenolle M, Madec G, Fichefet T, Flavoni S, Barthélemy A, et al. The Louvain-La-Neuve sea ice model LIM3.6: global and regional capabilities. Geosci Model Dev. 2015;8(10):2991–3005. https://doi.org/10.5194/gmd-8-2991-2015.

Runge J, Nowack P, Kretschmer M, Flaxman S, Sejdinovic D. Detecting and quantifying causal associations in large nonlinear time series datasets. Sci Adv. 2019;5(11):eaau4996. https://doi.org/10.1126/sciadv.aau4996.

Schott FA, Xie SP, McCreary Jr JP. Indian Ocean circulation and climate variability. Reviews of Geophysics. 2009;47:RG1002. https://doi.org/10.1029/2007RG000245.

Schreiber T. Measuring information transfer. Phys Rev Lett. 2000;85(2):461–464. https://doi.org/10.1103/PhysRevLett.85.461.

Sen PK. Estimates of the regression coefficient based on Kendall's tau. J Am Stat Assoc. 1968;63(324):1379–1389. https://doi.org/10.1080/01621459.1968.10480934.

Sprintall J, Wijffels SE, Molcard R, Jaya I. Direct estimates of the Indonesian Throughflow entering the Indian Ocean: 2004-2006. J Geophys Res Oceans. 2009;114:C07001. https://doi.org/10.1029/2008JC005257.

Stommel H. The westward intensification of wind-driven ocean currents. Eos, Transactions American Geophysical Union. 1948;29(2):202–206. https://doi.org/10.1029/TR029i002p00202.

Stommel H. Thermohaline Convection with Two Stable Regimes of Flow. Tellus. 1961;13(2):224–230. https://doi.org/10.3402/tellusa.v13i2.9491.

Storto A, Masina S, Navarra A. Evaluation of the CMCC eddy-permitting global ocean physical reanalysis system (C-GLORS, 1982–2012) and its assimilation components. Q J R Meteorol Soc. 2016;142(695):738–758. https://doi.org/10.1002/qj.2673.

Sugihara G, May R, Ye H, Hsieh CH, Deyle E, Fogarty M, et al. Detecting causality in complex ecosystems. Science. 2012;338(6106):496–500. https://doi.org/10.1126/science.1227079.

Sun S, Thompson AF. Centennial Changes in the Indonesian Throughflow Connected to the Atlantic Meridional Overturning Circulation. Geophys Res Lett. 2020;47:e2020GL090615. https://doi.org/10.1029/2020GL090615.

Theil H. A rank-invariant method of linear and polynomial regression analysis. Proceedings of the Koninklijke Nederlandse Akademie van Wetenschappen. 1950;53:386–392 (Part I), 521–525 (Part II), 1397–1412 (Part III). https://mathscinet.ams.org/mathscinet-getitem?mr=0036489.

Thornalley DJR, et al. Anomalously weak Labrador Sea convection and Atlantic overturning during the past 150 years. Nature. 2018;556:227–230. https://doi.org/10.1038/s41586-018-0007-4.

Tian T, Cheng L, Wang G, Abraham J, Wei W, Ren S, et al. Reconstructing ocean subsurface salinity at high resolution using a machine learning approach. Earth System Science Data. 2022;14(11):5037–5060. https://doi.org/10.5194/essd-14-5037-2022.

Torrence C, Compo GP. A Practical Guide to Wavelet Analysis. Bull Amer Meteor Soc. 1998;79(1):61–78. https://doi.org/10.1175/1520-0477(1998)079⟨0061:APGTWA⟩2.0.CO;2.

Torrence C, Webster PJ. Interdecadal Changes in the ENSO-Monsoon System. J Clim. 1999;12(8):2679–2690. https://doi.org/10.1175/1520-0442(1999)012⟨2679:ICITEM⟩2.0.CO;2.

Tozer B, Sandwell DT, Smith WHF, Olson C, Beale JR, Wessel P. Global Bathymetry and Topography at 15 Arc Sec: SRTM15+. Earth Space Sci. 2019;6(10):1847–1864. https://doi.org/10.1029/2019EA000658.

Vancoppenolle M, Bouillon S, Fichefet T, Goosse H, Lecomte O, Maqueda MAM, et al.: LIM: The Louvain-la-Neuve sea Ice Model. Note du Pole de modélisation, Institut Pierre-Simon Laplace (IPSL) No. 31; 2012. https://cmc.ipsl.fr/images/publications/scientific_notes/lim3_book.pdf (Accesed on May 27, 2025).

Virtanen P, Gommers R, Oliphant TE, Haberland M, Reddy T, Cournapeau D, et al. SciPy 1.0: Fundamental Algorithms for Scientific Computing in Python. Nature Methods. 2020;17:261–272. https://doi.org/10.1038/s41592-019-0686-2.

Waters J, Lea DJ, Martin MJ, Mirouze I, Weaver A, While J. Implementing a variational data assimilation system in an operational 1/4 degree global ocean model. Q J R Meteorol Soc. 2015;141(687):333–349. https://doi.org/10.1002/qj.2388.

Weijer W, Cheng W, Garuba OA, Hu A, Nadiga BT. CMIP6 models predict significant 21st century decline of the Atlantic Meridional Overturning Circulation. Geophys Res Lett. 2019;46:12360–12368. https://doi.org/10.1029/2019GL085075.

Wessel P, Luis JF, Uieda L, Scharroo R, Wobbe F, Smith WHF, et al. The Generic Mapping Tools Version 6. Geochem Geophys Geosyst. 2019;20(11):5556–5564. https://doi.org/10.1029/2019GC008515.

van Westen RM, Kliphuis M, Dijkstra HA. Physics-based early warning signal shows that AMOC is on tipping course. Sci Adv. 2024;10(6):eadk1189. https://doi.org/10.1126/sciadv.adk1189.

Wyrtki K. Physical oceanography of the Southeast Asian waters. NAGA Report. 1961;2:1–195. Scientific Results of Marine Investigations of the South China Sea and the Gulf of Thailand.

Ye H, Deyle ER, Gilarranz LJ, Sugihara G. Distinguishing time-delayed causal interactions using convergent cross mapping. Sci Rep. 2015;5:14750. https://doi.org/10.1038/srep14750.

Zuo H, Balmaseda MA, Mogensen K. The new eddy-permitting ORAP5 ocean reanalysis: description, evaluation and uncertainties in climate signals. Clim Dyn. 2017;49:791–811. https://doi.org/10.1007/s00382-015-2675-1.